The Astrophysical Journal, 856:126 (18pp), 2018 April 1 https://doi.org/10.3847/1538-4357/aab043

The Next Generation Virgo Cluster Survey (NGVS). XVIII. Measurement and Calibration of Surface Brightness Fluctuation Distances for Bright Galaxies in Virgo (and Beyond)

Michele Cantiello[1], John P. Blakeslee[2], Laura Ferrarese[2,3], Patrick Côté[2], Joel C. Roediger[2], Gabriella Raimondo[1], Eric W. Peng[4,5], Stephen Gwyn[2], Patrick R. Durrell[6], and Jean-Charles Cuillandre[7]
[1] INAF Osservatorio Astronomico d'Abruzzo, via Maggini, snc, I-64100, Italy; cantiello@oa-teramo.inaf.it
[2] National Research Council of Canada, Herzberg Astronomy and Astrophysics Research Centre, Victoria, BC, Canada
[3] Gemini Observatory, Northern Operations Center, 670 N. A'ohoku Place, Hilo, HI 96720, USA
[4] Department of Astronomy, Peking University, Beijing 100871, People's Republic of China
[5] Kavli Institute for Astronomy and Astrophysics, Peking University, Beijing 100871, People's Republic of China
[6] Department of Physics and Astronomy, Youngstown State University, Youngstown, OH 44555, USA
[7] AIM Paris Saclay, CNRS/INSU, CEA/Irfu, Université Paris Diderot, Orme des Merisiers, France
Received 2017 October 26; revised 2018 February 14; accepted 2018 February 14; published 2018 March 30

Abstract

We describe a program to measure surface brightness fluctuation (SBF) distances to galaxies observed in the Next Generation Virgo Cluster Survey (NGVS), a photometric imaging survey covering 104 deg^2 of the Virgo cluster in the u^*, g, i, and z bandpasses with the Canada–France–Hawaii Telescope. We describe the selection of the sample galaxies, the procedures for measuring the apparent i-band SBF magnitude $\overline{m}_i$, and the calibration of the absolute $\overline{M}_i$ as a function of observed stellar population properties. The multiband NGVS data set provides multiple options for calibrating the SBF distances, and we explore various calibrations involving individual color indices as well as combinations of two different colors. Within the color range of the present sample, the two-color calibrations do not significantly improve the scatter with respect to wide-baseline, single-color calibrations involving u^*. We adopt the $(u^* - z)$ calibration as a reference for the present galaxy sample, with an observed scatter of 0.11 mag. For a few cases that lack good u^* photometry, we use an alternative relation based on a combination of $(g - i)$ and $(g - z)$ colors, with only a slightly larger observed scatter of 0.12 mag. The agreement of our measurements with the best existing distance estimates provides confidence that our measurements are accurate. We present a preliminary catalog of distances for 89 galaxies brighter than $B_T \approx 13.0$ mag within the survey footprint, including members of the background M and W Clouds at roughly twice the distance of the main body of the Virgo cluster. The extension of the present work to fainter and bluer galaxies is in progress.

Key words: distance scale – galaxies: clusters: individual (Virgo) – galaxies: distances and redshifts

1. Introduction

Reliable distance estimation is an essential prerequisite for knowledge of the fundamental characteristics of structures in the universe, including their size, luminosity, and mass. Measurement of significant samples of high-quality galaxy distances can enable mapping of large-scale structures and velocity fields in the nearby universe, where the peculiar velocity is often a substantial fraction of the redshift. Resolving the 3D structure of galaxies within clusters requires measurement precision for individual galaxies better than the ratio of the cluster depth to its mean distance, or errors <0.1 mag even for Virgo and Fornax, the only galaxy clusters within $\approx$20 Mpc (Mei et al. 2007; Blakeslee et al. 2009, hereafter B09).

There are very few extragalactic distance indicators that are both capable of this level of precision, and able to be applied to a large fraction of galaxies within a given environment. For instance, the extensive review by Freedman & Madore (2010) discusses "six high-precision (extragalactic) distance-determination methods," namely, Cepheid variables, the tip of the red giant branch (TRGB), water masers, the Tully–Fisher (TF) relation, Type Ia supernovae (SNe Ia), and surface brightness fluctuations (SBFs). The first three of these methods require high spatial resolution and have mainly been used for nearby galaxies, i.e., at distances $\lesssim$20 Mpc where peculiar velocities are comparable to the *Hubble* velocity; they have been used to calibrate the latter three methods, which have ranges extending out into the *Hubble* flow.

Most of the precision methods reviewed by Freedman & Madore (2010) have been applied to measure distances of galaxies in the Virgo cluster, thanks to its proximity, with the exception being the water masers, which are very rare. However, not all of the methods are practical for mapping the 3D structure of the cluster. For instance, Cepheids bolster the rung of the ladder by which our knowledge of distances ascends from the solar neighborhood to the realm of the galaxies. However, at extragalactic distances, Cepheids require many epochs of deep, high-resolution observations and are only found within star-forming galaxies, not in the early-type galaxies that populate dense environments. The TF relation has traditionally produced distance errors $\gtrsim$0.3 mag, much larger than the depth of the Virgo cluster, but as Freedman & Madore (2010) discuss, the precision is vastly improved when using 3.6 μm photometry. However, again the method works best for spiral galaxies, rather than cluster ellipticals. On the other hand, Type Ia supernovae (SNe Ia) occur in all galaxy types and are highly luminous, making them easily observable in the nearby universe. However, they are rare events; according to the NASA/IPAC Extragalactic Database (NED),[8] the last SNe Ia to occur in the Virgo cluster cD galaxy M87 was a century ago, SN 1919A, and no confirmed

[8] http://ned.ipac.caltech.edu

SNe Ia have occurred in the brightest cluster galaxy M49, despite its enormous stellar mass. The TRGB method is also applicable to all types of galaxies, but very deep high-resolution imaging is required to reach a sufficient depth along the RGB in external galaxies; consequently, very few galaxies in the Virgo cluster have TRGB distance estimates (Durrell et al. 2007; Bird et al. 2010; Lee & Jang 2017).

Other methods with the potential for mapping the Virgo cluster region include Mira variables (e.g., Whitelock et al. 2008) and the globular cluster luminosity function (GCLF; e.g., Harris 1991). Miras are luminous asymptotic giant branch stars, especially bright in the infrared, and likely present in most galaxies. However, like the other resolved stellar photometry methods, Miras require very high spatial resolution and much longer temporal baselines then Cepheids. Thus far, this method has only been used to distances of a few megaparsec (Rejkuba 2004), but it may become much more far-reaching with the combination of *Gaia* and the *James Webb Space Telescope* (*JWST*). *Gaia* is expected to measure parallaxes for ∼40,000 Miras (Robin et al. 2012), and *JWST* will operate in the near- and mid-IR regime, where Miras reach magnitudes brighter than ≈−8 mag (Feast & Whitelock 2014, ≈−9.2 mag at 8 μm). GCLF measurements have been made for large samples of galaxies in the Virgo and Fornax clusters (Jordán et al. 2006; Villegas et al. 2010), but in addition to the established trends with host galaxy luminosity, the distance indicator likely depends in complex ways on galaxy environment and dynamical history (e.g., Rejkuba 2012). Overall, it appears to be a less precise method than the others mentioned above, especially for galaxies with small or modest GC populations.

Among the available extragalactic distance indicators, the SBF method, introduced by Tonry & Schneider (1988), is the only distance indicator with high enough precision and wide enough applicability to have clearly resolved the depth of the Virgo cluster (West & Blakeslee 2000; Mei et al. 2007) and detected the depth of the more compact Fornax cluster (B09). This does not mean it is the most precise indicator, only that it is the best suited for this particular problem. The reason is that, unlike Cepheids or the TRGB, the SBF method does not require resolved stellar photometry, but like those methods, it relies on well-understood stellar physics and can be calibrated from stellar population observables, rather than assuming an empirical scaling law or a supposed universal luminosity function. In addition, unlike the SNe Ia or maser methods, it is based on a phenomenon present in all galaxies (though with a predictability depending on stellar population; see the review by Blakeslee 2012).

For early-type galaxies, or the relatively "clean" regions of spirals without significant dust or recent star formation, if the data are of sufficient depth for the SBF signal to exceed the photometric noise, then the limiting factor is the ability to detect and remove faint sources, especially globular clusters (GCs), that contaminate the power spectrum of the fluctuations. Excellent seeing and high signal-to-noise greatly facilitate the rejection of such contaminants, and therefore improve the precision of the method. The SBF work by Mei et al. (2007) on the 3D structure of Virgo used data of exquisite quality from the ACS Virgo Cluster Survey (ACSVCS; Côté et al. 2004), a Large Program with the *Hubble Space Telescope* (*HST*). However, as groundbreaking as that survey was, its 100 ACS pointings included less than half of the early-type Virgo members with B magnitude $B_T < 16$ mag (though a complete sample of the ≈20 brightest), and therefore the mapping of the early-types was necessarily incomplete. For complete areal coverage, one must resort to wide-field imaging from the ground. The only previous major ground-based SBF survey was by Tonry et al. (1997, 2001), which reported distances of variable precision, acquired in the I band under conditions of highly variable quality, for ≈300 galaxies out to about 40 Mpc, including 31 in the Virgo cluster. There have been major advances in both CCD cameras and in the efficiency of observatory operations since the observations were conducted for that seminal survey more than 20 years ago; these advances greatly increase the potential of the SBF method and make it well worth revisiting today. In fact, Tonry et al. (2001) hypothesized a future survey that would repeat the SBF measurements for all the same galaxies in only one-fourth of the integration time and yield distances with 40% better precision because it would be conducted with a median seeing of $\lesssim$0.″6, instead of ≈0.″9.

The Next Generation Virgo Cluster Survey (NGVS; Ferrarese et al. 2012) is a Large Program with the 1-deg^2 MegaCam imager at the MegaPrime focus of the Canada–France–Hawaii Telescope (CFHT). In 117 pointings (not including background fields), it covers a contiguous 104 deg^2 of the Virgo cluster, out to the virial radii for both the Virgo A and B subclusters, in the u^*, g, i, and z bandpasses. It supersedes all previous optical studies of Virgo and leverages a large amount of spectroscopic follow up and auxiliary data at other wavelengths to address important questions about the galaxy luminosity function, scaling relations, stellar populations, dynamical interactions, GCs, galactic nuclei, and the growth of the cluster itself. The NGVS project motivations, strategy, and observational program are discussed in detail by Ferrarese et al. (2012).

The NGVS observations were designed to deliver stacked images in the i band with seeings of 0.″6 or better to enable high-quality measurement of the i-band SBF magnitude $\overline{m}_i$ for the greatest number of galaxies. The wide-baseline photometry, from u^* to z, also enables accurate characterization of the galaxy stellar populations, required for calibrating the absolute SBF magnitude $\overline{M}_i$. The goal of the SBF component of the NGVS project is to use the resulting distance moduli ($\overline{m}_i - \overline{M}_i$) to produce the most detailed possible 3D map of the cluster. In the present work, we present the first set of SBF measurements for 89 galaxies brighter than $B_T \approx 13$ mag. The following section briefly describes the NGVS imaging and data reductions. Section 3 details our SBF measurement procedures, while in Section 4 we derive multiple calibrations based on various photometric colors and apply the calibrations to determine the galaxy distances. The distances are tabulated and discussed in Section 5, where we also compare our results with previous measurements and stellar population model predictions. Section 6 provides a summary.

2. NGVS Data, Galaxy Sample, and Distance Zero Point

This work is based entirely on CFHT/MegaCam imaging data from the NGVS. Full details on the NGVS survey observations and image processing are presented in Ferrarese et al. (2012); here we provide only a brief summary of the relevant details. The NGVS exploits the capabilities of CFHT/MegaCam to reach 5σ limiting magnitudes for point source detection of 26.3, 26.6, 25.8, and 24.8 mag in the stacked u^*, g, i, and z images, respectively, across the entire Virgo cluster. This is well beyond the turnover for the GCLF (e.g., Durrell et al. 2014), even when the GCs are superimposed on a bright galaxy background. The images are therefore well-suited for

Table 1
Sample Properties

VCC	R.A. (J2000) (deg)	Decl. (J2000) (deg)	B_T (mag)	cz km s^{-1}	$(m - M)_{ACS}$ (mag)	T_{type}	Alt. Name
49	183.071933	13.205196	12.2	2273	⋯	−4.90 ± 0.40	NGC 4168
167	183.976608	13.149457	11.0	131	⋯	3.00 ± 0.50	NGC 4216
199	184.140781	7.462067	12.9	2584	⋯	1.00 ± 0.30	NGC 4224
220	184.282006	7.624276	13.0	2275	⋯	−2.00 ± 0.50	NGC 4233
222	184.291184	7.191575	12.7	2263	⋯	1.00 ± 0.40	NGC 4235
226	184.297607	15.324038	12.5	864	⋯	4.00 ± 0.50	NGC 4237
341	184.842724	6.098672	12.7	1777	⋯	1.00 ± 0.50	NGC 4260
345	184.846746	5.824897	11.3	2177	⋯	−4.80 ± 0.40	NGC 4261
355	184.877385	14.877653	12.4	1359	30.95 ± 0.07	−2.60 ± 0.70	NGC 4262
369	184.938669	12.798262	11.8	1021	31.00 ± 0.07	−2.70 ± 0.70	NGC 4267
483	185.386537	14.606137	12.1	1125	⋯	5.10 ± 0.60	NGC 4298
523	185.517183	12.787498	13.1	1520	⋯	−2.00 ± 0.70	NGC 4306
524	185.523566	9.043656	12.8	1055	⋯	3.20 ± 0.70	NGC 4307
559	185.630565	15.537915	12.6	158	⋯	2.10 ± 0.90	NGC 4312
570	185.660603	11.800900	12.7	1432	⋯	2.10 ± 0.40	NGC 4313
596	185.728792	15.822282	10.1	1571	⋯	4.00 ± 0.30	NGC 4321, M 100
613	185.775720	5.250345	12.6	1665	⋯	−0.80 ± 1.20	NGC 4324
648	185.895606	6.081775	12.3	1266	⋯	−4.60 ± 1.00	NGC 4339
654	185.897017	16.722345	11.6	933	⋯	−1.20 ± 0.60	NGC 4340
657	185.912504	7.053998	12.6	761	⋯	−3.20 ± 1.00	NGC 4342
685	185.991010	16.693338	11.2	1210	⋯	−1.80 ± 0.90	NGC 4350
692	186.006313	12.204766	13.0	2303	⋯	2.80 ± 1.70	NGC 4351
731	186.117730	7.317770	10.5	1243	31.82 ± 0.07	−4.80 ± 0.40	NGC 4365
759	186.230973	11.704197	11.8	933	31.14 ± 0.07	−1.30 ± 0.60	NGC 4371
763	186.265603	12.886976	10.3	1017	31.34 ± 0.07	−4.40 ± 1.20	NGC 4374, M 084
778	186.301410	14.762169	12.7	1338	31.24 ± 0.07	−2.60 ± 0.60	NGC 4377
784	186.311442	15.607421	12.7	1074	31.00 ± 0.07	−2.70 ± 0.60	NGC 4379
792	186.342391	10.016793	12.4	949	⋯	2.40 ± 0.90	NGC 4380
828	186.423673	12.810517	12.8	538	31.28 ± 0.07	−4.80 ± 0.60	NGC 4387
873	186.529766	13.111997	12.6	237	⋯	3.20 ± 0.80	NGC 4402
874	186.529812	16.180971	13.0	1735	⋯	0.30 ± 1.10	NGC 4405
881	186.548981	12.946240	10.1	−224	31.26 ± 0.07	−4.80 ± 0.50	NGC 4406, M 086
912	186.634391	12.610708	12.4	91	⋯	2.10 ± 1.10	NGC 4407
929	186.668694	8.435697	13.1	907	⋯	−0.90 ± 2.10	NGC 4415
944	186.710867	9.584259	12.1	828	31.02 ± 0.07	−1.90 ± 0.50	NGC 4417
958	186.735107	15.047303	12.1	−261	⋯	1.20 ± 0.90	NGC 4419
966	186.760585	15.461466	12.4	1551	⋯	−0.50 ± 0.80	NGC 4421
979	186.798630	9.420773	12.3	437	⋯	0.90 ± 0.50	NGC 4424
984	186.805580	12.734765	12.3	1892	⋯	−0.60 ± 1.20	NGC 4425
1003	186.860486	11.107684	11.2	1104	⋯	−0.80 ± 1.50	NGC 4429
1025	186.902832	8.154342	13.1	1070	31.76 ± 0.07	−4.70 ± 0.70	NGC 4434
1030	186.918717	13.078984	11.8	791	31.11 ± 0.07	−2.10 ± 0.50	NGC 4435
1043	186.940202	13.008874	10.5	71	⋯	0.60 ± 1.50	NGC 4438
1062	187.016147	9.803712	11.4	547	30.93 ± 0.07	−1.90 ± 0.40	NGC 4442
1110	187.123295	17.085020	10.9	1954	⋯	2.40 ± 0.70	NGC 4450
1125	187.180447	11.755032	12.5	162	⋯	−1.90 ± 0.80	NGC 4452
1146	187.239835	13.241934	12.9	677	31.06 ± 0.07	−4.90 ± 0.40	NGC 4458
1154	187.250163	13.978475	11.4	1192	31.02 ± 0.07	−1.60 ± 1.10	NGC 4459
1158	187.262550	13.183801	11.5	1924	⋯	−0.70 ± 1.30	NGC 4461
1190	187.366793	8.749803	12.2	588	⋯	0.20 ± 0.70	NGC 4469
1226	187.444854	8.000490	9.3	981	31.12 ± 0.07	−4.80 ± 0.50	NGC 4472, M 049
1231	187.453625	13.429436	11.1	2244	30.92 ± 0.07	−4.70 ± 0.70	NGC 4473
1242	187.473118	14.068584	12.6	1611	30.95 ± 0.08	−1.90 ± 0.90	NGC 4474
1250	187.496153	12.348719	12.9	1959	31.24 ± 0.08	−2.90 ± 1.00	NGC 4476
1253	187.509172	13.636533	11.3	1338	⋯	−1.70 ± 0.70	NGC 4477
1279	187.572571	12.328559	12.2	1349	31.16 ± 0.07	−4.90 ± 0.40	NGC 4478
1303	187.669345	9.015672	13.1	884	31.12 ± 0.07	−1.40 ± 0.70	NGC 4483
1316	187.705937	12.391122	9.6	1284	31.11 ± 0.08	−4.30 ± 0.60	NGC 4486, M 087
1318	187.714059	8.360007	12.9	980	⋯	−0.10 ± 0.60	NGC 4488
1321	187.717714	16.758843	12.8	940	30.93 ± 0.07	−4.70 ± 0.90	NGC 4489
1368	187.885575	11.624746	12.7	1042	⋯	−1.10 ± 1.10	NGC 4497
1412	188.025974	11.176390	12.1	1334	⋯	−1.70 ± 1.80	NGC 4503
1535	188.512433	7.699310	10.0	617	⋯	−1.90 ± 0.40	NGC 4526

Table 1
(Continued)

VCC	R.A. (J2000) (deg)	Decl. (J2000) (deg)	B_T (mag)	cz km s^{-1}	$(m-M)_{ACS}$ (mag)	T_{type}	Alt. Name
1537	188.525321	11.321253	12.7	1378	30.98 ± 0.07	−2.00 ± 0.50	NGC 4528
1552	188.566164	13.075314	12.6	90	⋯	−0.10 ± 2.40	NGC 4531
1588	188.711889	15.551642	12.5	1274	⋯	6.20 ± 0.90	NGC 4540
1615	188.860251	14.496350	11.0	486	⋯	3.10 ± 0.50	NGC 4548, M 091
1619	188.877428	12.220753	12.5	459	30.93 ± 0.07	−2.00 ± 0.70	NGC 4550
1630	188.908131	12.263988	12.9	1176	31.05 ± 0.07	−4.90 ± 0.40	NGC 4551
1632	188.915884	12.556365	10.8	340	31.02 ± 0.07	−4.60 ± 0.90	NGC 4552, M 089
1664	189.112434	11.439228	12.0	1142	31.01 ± 0.07	−4.60 ± 0.70	NGC 4564
1692	189.222419	7.246580	11.8	1787	31.17 ± 0.07	−1.90 ± 1.00	NGC 4570
1720	189.377334	9.555100	12.3	2292	31.07 ± 0.07	−2.10 ± 0.60	NGC 4578
1727	189.431389	11.818205	10.6	1517	⋯	2.80 ± 0.60	NGC 4579, M 058
1730	189.451619	5.368521	12.6	1035	⋯	1.60 ± 0.70	NGC 4580
1813	189.983154	10.176147	11.5	1892	⋯	−0.80 ± 0.80	NGC 4596
1859	190.239811	11.912173	12.7	1640	⋯	0.60 ± 1.40	NGC 4606
1869	190.305385	10.155651	12.1	1850	⋯	−1.70 ± 0.80	NGC 4608
1883	190.386455	7.314879	12.6	1775	31.09 ± 0.07	−2.00 ± 0.40	NGC 4612
1903	190.509428	11.646945	10.8	467	30.86 ± 0.07	−4.80 ± 0.40	NGC 4621, M 059
1938	190.697623	11.442507	12.1	1152	31.19 ± 0.07	−2.60 ± 0.70	NGC 4638
1978	190.916532	11.552700	9.8	1110	31.08 ± 0.08	−4.60 ± 0.90	NGC 4649, M 060
1999	191.122489	13.498557	13.1	469	⋯	0.00 ± 0.50	NGC 4659
2000	191.133259	11.190501	11.9	1083	30.88 ± 0.07	−4.60 ± 0.70	NGC 4660
2058	191.939846	13.762808	11.6	1604	⋯	4.70 ± 0.90	NGC 4689
2066	192.063007	10.983284	12.2	1160	⋯	−1.80 ± 0.70	NGC 4694
2087	192.778237	10.912097	12.2	925	⋯	−3.60 ± 1.30	NGC 4733
2092	193.072900	11.313863	11.5	1351	31.03 ± 0.07	−2.40 ± 1.10	NGC 4754
2095	193.233227	11.230975	10.8	986	⋯	−1.80 ± 0.90	NGC 4762

SBF analysis, as most of the potentially contaminating sources can be identified and removed.

Individual exposures in the NGVS survey were processed with Elixir-LSB, a variant of the Elixir processing pipeline (Magnier & Cuillandre 2004) specifically designed for the NGVS observing strategy, that accurately removes background variations using sky frames constructed from adjacent fields observed as part of a multi-pointing "step-dither" sequence. The processed exposures for a given pointing were then stacked using a variant of the MegaPipe (Gwyn 2008) pipeline. In addition to removing scattered light, this procedure effectively removes the sky fringing in the final *i*-band images, and nearly eliminates it in *z*. This is important because residual fringing can contaminate the image power spectrum and cause major problems for the SBF analysis in ground-based data (e.g., Tonry et al. 1997). As a result of the excellent detrending and sky subtraction with Elixir-LSB and the optimized stacking by MegaPipe, the respective surface brightness limits (2-σ) in u^*, g, i, and z are 29.3, 29.0, 27.4, and 26.0 mag arcsec^{-2}. As discussed in Ferrarese et al. (2012), the image processing was somewhat different for the central 4 deg^2 "pilot region," which was observed before the final observing procedure was devised. However, experiments comparing our final results for the same fields using the different processings showed negligible differences.

For this first paper of the NGVS-SBF project, we have selected the complete sample of galaxies brighter than $B_T \approx 13$ in the Virgo Cluster Catalog (VCC) of Binggeli et al. (1985), and falling within the 104 deg^2 NGVS footprint. This initial sample of bright galaxies has allowed us to optimize our SBF measurement procedures for NGVS data and, as detailed in Section 4, establish the behavior of the *i*-band SBF magnitude over a broad range of integrated galaxy colors. The SBF analysis for a larger sample of fainter galaxies is in progress and will be presented in a future work. Table 1 lists the sample galaxies included in the present work. For each galaxy, we give the VCC number from Binggeli et al. (1985); celestial coordinates (J2000) in degrees; total B_T magnitude from the VCC; heliocentric velocity from NED; ACSVCS SBF distance modulus $(m-M)_{ACS}$ as tabulated by B09, when available; morphological T_{type} from Hyperleda (Makarov et al. 2014); and the alternative NGC and Messier names.

The availability of the $(m-M)_{ACS}$ for ≈40% of the sample galaxies makes it possible to set the distance zero point for our NGVS SBF measurements. The mean distance modulus for the 85 galaxies in the Virgo cluster proper (excluding the background W′ group and the foreground NGC 4697) from B09 is 31.092 ± 0.013, or 16.5 ± 0.1 Mpc. This is the same mean distance as used in all previous NGVS papers. The zero point for the ACSVCS distances comes from assuming the Tonry et al. (2001) mean distance for 31 Virgo galaxies, revised by −0.06 mag (Blakeslee et al. 2002) based on comparison to the final set of Key Project Cepheid distances from Freedman et al. (2001). With improvements in the precision of the Cepheid zero point (Freedman & Madore 2010), the systematic uncertainty in this mean distance is approximately 0.1 mag, or ≈0.8 Mpc, consistent with the agreement with the predicted zero point from the SPoT stellar population models (Raimondo et al. 2005; Raimondo 2009; see the discussion by Blakeslee et al. 2010).

3. SBF Measurements

For measuring the SBF amplitudes in the sample galaxies, we adopt the same basic procedures already developed in previous works and described in detail elsewhere (Blakeslee et al. 2001, 2009, 2010; Cantiello et al. 2005, 2007a, 2007b,

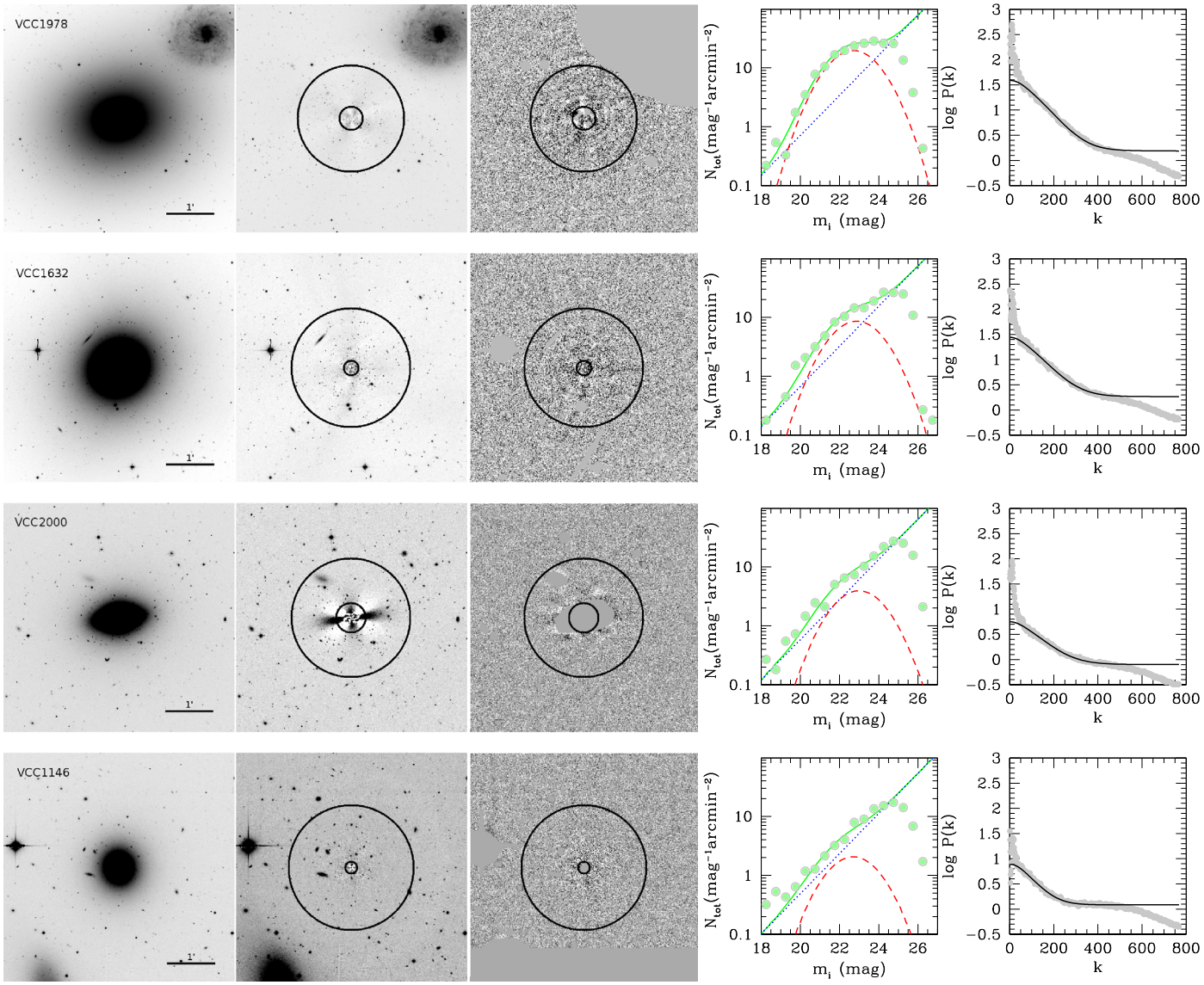

Figure 1. SBF analysis images and plots for a selection of galaxies, as labeled. Starting from the left: *i*-band image, residual, and residual masked image (first to third panel). The black annuli in the second and third panels show the inner and outer radii of the region adopted for SBF measurements. Fourth panel: fitted luminosity function of external sources. Filled green circles mark observational data; the solid green curve is the best fit to the data; the two components of the total luminosity function, i.e., the background galaxies and the GCLF, are shown with a blue dotted and a red dashed curve, respectively. Fifth panel: azimuthal average of the residual image power spectrum (gray dots) and the fit obtained according to the procedure described in the text (solid black curve).

2011a, 2013; Mei et al. 2005a, 2005b), including both *HST* and ground-based studies. In broad terms, the SBF distance measurement entails: (a) modeling and subtracting of the 2D galaxy surface brightness distribution and the large-scale model residuals to obtain a clean residual image; (b) masking of contaminating sources (stars, background galaxies, and especially GCs in the galaxy itself) down to a known threshold; (c) creating an accurate point-spread function (PSF) template for the image; (d) determining the amplitude of the power spectrum in Fourier space on the scale of PSF, which causes correlation of the fluctuations in adjacent pixels; (e) estimating the "residual variance" from contaminating sources remaining in the masked image and subtracting this variance from the power spectrum amplitude to obtain the corrected SBF magnitude $\overline{m}$; (f) adopting a value for $\overline{M}$ from either an empirical or theoretical SBF calibration (generally based on galaxy color) to obtain the distance modulus, $\overline{m} - \overline{M}$.

For this NGVS SBF analysis, we adopted the sky background estimates and galaxy isophotal models described by Ferrarese et al. (2012). The large-scale residuals, still present in the frame after subtracting the galaxy model, were removed using the background map obtained with SExtractor (Bertin & Arnouts 1996) adopting a mesh size ≈10 times the FWHM (Tonry et al. 1990; Cantiello et al. 2005). We refer to the image with the sky, galaxy model, and large-scale residuals all subtracted as the residual frame. The photometry of the external sources (stars, background galaxies, and GCs) was done by running SExtractor on the residual frame after masking saturated stars, very extended galaxies, and other large features that could be problematic for SExtractor. We used an input weight image that included the galaxy photometric noise as well as additional variance caused by the SBF (for details, see Jordán et al. 2004; Cantiello et al. 2005) to avoid detecting the fluctuations as objects themselves. The SExtractor MAG_AUTO measurements include roughly 90% of

Table 2
SBF and Color Measurements

VCC	Area (arcmin^2)	⟨Rad⟩ (arcsec)	$(u^* - z)$ (mag)	$(g - i)$ (mag)	$(g - z)$ (mag)	$\overline{m_i}$ (mag)	$(m - M)$[a] (mag)	D (Mpc)	Comment[b]
0049	4.11	51.5	2.623 ± 0.007	0.983 ± 0.002	1.214 ± 0.007	31.63 ± 0.09	32.49 ± 0.13	31.4 ± 1.9	M
0167	1.05	59.2	2.501 ± 0.030	0.999 ± 0.013	1.234 ± 0.029	30.30 ± 0.14	31.29 ± 0.23	18.1 ± 1.9	V
0199	0.38	31.2	2.568 ± 0.012	0.989 ± 0.005	1.211 ± 0.010	30.76 ± 0.07	31.66 ± 0.13	21.5 ± 1.3	W/W′?
0220	1.02	32.9	2.737 ± 0.008	1.033 ± 0.004	1.302 ± 0.007	31.75 ± 0.12	32.46 ± 0.15	31.1 ± 2.2	W
0222	0.37	28.0	2.546 ± 0.015	0.965 ± 0.006	1.209 ± 0.012	31.21 ± 0.15	32.12 ± 0.19	26.6 ± 2.4	W
0226	0.64	54.5	2.171 ± 0.042	0.816 ± 0.012	1.069 ± 0.041	30.04 ± 0.08	31.38 ± 0.23	18.9 ± 2.0	V
0341	0.64	39.6	2.632 ± 0.027	1.002 ± 0.004	1.266 ± 0.025	31.32 ± 0.11	32.14 ± 0.20	26.8 ± 2.5	W
0345	6.18	64.3	2.796 ± 0.007	1.075 ± 0.001	1.378 ± 0.007	31.67 ± 0.12	32.31 ± 0.15	29.0 ± 2.0	W
0355	0.48	33.0	2.667 ± 0.009	1.013 ± 0.003	1.281 ± 0.008	29.87 ± 0.05	30.69 ± 0.11	13.7 ± 0.7	V
0369	2.96	45.4	2.815 ± 0.005	1.106 ± 0.007	1.346 ± 0.008	30.32 ± 0.04	30.99 ± 0.09	15.7 ± 0.6	V
0483	1.26	64.6	2.183 ± 0.036	0.749 ± 0.014	0.978 ± 0.035	29.59 ± 0.06	30.92 ± 0.21	15.3 ± 1.5	V
0523	1.82	32.2	2.308 ± 0.010	0.895 ± 0.005	1.076 ± 0.010	30.11 ± 0.06	31.32 ± 0.12	18.4 ± 1.1	V
0524	0.54	27.8	2.323 ± 0.017	0.900 ± 0.008	1.104 ± 0.016	29.85 ± 0.07	31.01 ± 0.15	15.9 ± 1.1	V
0559	1.25	36.4	2.194 ± 0.015	0.866 ± 0.005	1.050 ± 0.014	29.72 ± 0.09	31.03 ± 0.16	16.1 ± 1.2	V
0570	0.46	30.1	2.351 ± 0.015	0.867 ± 0.011	1.104 ± 0.015	29.99 ± 0.09	31.15 ± 0.16	17.0 ± 1.2	V
0596	4.11	179.0	2.087 ± 0.036	0.767 ± 0.012	1.052 ± 0.036	29.75 ± 0.06	31.17 ± 0.21	17.2 ± 1.7	V
0613	0.33	33.3	2.225 ± 0.020	0.976 ± 0.009	1.183 ± 0.018	29.68 ± 0.07	30.95 ± 0.16	15.5 ± 1.2	V
0648	1.01	28.9	2.764 ± 0.004	1.061 ± 0.001	1.320 ± 0.004	31.07 ± 0.06	31.75 ± 0.09	22.4 ± 0.9	W′
0654	3.37	54.7	⋯	1.020 ± 0.003	1.281 ± 0.010	30.25 ± 0.04	31.06 ± 0.14	16.3 ± 1.1	V
0657	0.35	27.1	2.435 ± 0.072	0.857 ± 0.017	1.070 ± 0.069	30.41 ± 0.12	31.45 ± 0.31	19.5 ± 2.7	W′
0685	3.67	55.3	⋯	0.983 ± 0.005	1.230 ± 0.020	30.02 ± 0.05	30.95 ± 0.20	15.5 ± 1.4	V
0692	0.54	43.0	1.936 ± 0.040	0.737 ± 0.030	0.866 ± 0.040	29.37 ± 0.07	30.96 ± 0.22	15.6 ± 1.6	V
0731	3.96	52.2	2.811 ± 0.000	1.067 ± 0.000	1.311 ± 0.000	31.15 ± 0.06	31.78 ± 0.06	22.7 ± 0.6	W′
0759	0.83	54.3	2.717 ± 0.008	1.069 ± 0.006	1.340 ± 0.007	30.30 ± 0.07	31.06 ± 0.12	16.3 ± 0.9	V
0763	5.91	61.5	2.866 ± 0.002	1.114 ± 0.001	1.371 ± 0.001	30.61 ± 0.04	31.22 ± 0.06	17.5 ± 0.5	V
0778	3.26	48.2	2.624 ± 0.016	1.010 ± 0.015	1.240 ± 0.021	30.33 ± 0.05	31.19 ± 0.14	17.3 ± 1.1	V
0784	3.22	46.0	2.650 ± 0.011	1.036 ± 0.004	1.259 ± 0.011	30.22 ± 0.04	31.02 ± 0.12	16.0 ± 0.9	V
0792	0.41	54.1	2.480 ± 0.017	0.963 ± 0.008	1.161 ± 0.016	30.01 ± 0.06	31.01 ± 0.15	15.9 ± 1.1	V
0828	1.20	33.3	2.639 ± 0.012	1.049 ± 0.006	1.261 ± 0.012	30.50 ± 0.08	31.33 ± 0.14	18.5 ± 1.2	V
0873	0.52	34.4	2.168 ± 0.016	0.874 ± 0.007	1.039 ± 0.015	29.73 ± 0.05	31.07 ± 0.14	16.4 ± 1.1	V
0874	0.39	32.4	2.205 ± 0.011	0.829 ± 0.005	1.030 ± 0.011	29.86 ± 0.07	31.15 ± 0.13	17.0 ± 1.0	V
0881	2.82	46.3	2.777 ± 0.001	1.058 ± 0.001	1.335 ± 0.001	30.69 ± 0.10	31.37 ± 0.10	18.8 ± 0.9	V
0912	0.96	52.5	2.278 ± 0.037	0.898 ± 0.017	1.063 ± 0.036	29.82 ± 0.08	31.05 ± 0.22	16.2 ± 1.6	V
0929	2.67	39.2	2.469 ± 0.013	0.909 ± 0.004	1.149 ± 0.012	29.97 ± 0.04	30.97 ± 0.12	15.7 ± 0.9	V
0944	2.11	49.5	2.371 ± 0.021	0.956 ± 0.007	1.181 ± 0.020	29.95 ± 0.11	31.06 ± 0.19	16.3 ± 1.4	V
0958	0.85	40.8	2.205 ± 0.025	0.918 ± 0.010	1.139 ± 0.024	29.98 ± 0.07	31.29 ± 0.18	18.1 ± 1.5	V
0966	1.78	38.7	⋯	0.947 ± 0.003	1.229 ± 0.005	30.09 ± 0.06	31.07 ± 0.13	16.4 ± 1.0	V
0979	0.25	43.3	2.019 ± 0.020	0.812 ± 0.007	0.970 ± 0.020	29.53 ± 0.10	31.02 ± 0.18	16.0 ± 1.3	V
0984	3.04	53.7	2.285 ± 0.046	0.946 ± 0.018	1.123 ± 0.045	29.79 ± 0.07	31.00 ± 0.24	15.9 ± 1.7	V
1003	4.68	61.1	2.766 ± 0.004	1.074 ± 0.002	1.388 ± 0.003	30.38 ± 0.04	31.08 ± 0.07	16.4 ± 0.6	V
1025	2.42	38.1	2.612 ± 0.009	0.976 ± 0.003	1.218 ± 0.009	30.78 ± 0.04	31.62 ± 0.11	21.1 ± 1.1	W′
1030	1.21	37.5	2.461 ± 0.005	0.975 ± 0.002	1.172 ± 0.005	30.10 ± 0.06	31.12 ± 0.10	16.8 ± 0.8	V
1043	1.84	77.5	2.398 ± 0.024	0.911 ± 0.011	1.231 ± 0.023	29.99 ± 0.07	31.08 ± 0.18	16.5 ± 1.3	V
1062	2.21	46.6	2.654 ± 0.005	1.045 ± 0.002	1.305 ± 0.005	29.98 ± 0.03	30.78 ± 0.08	14.3 ± 0.5	V
1110	1.62	80.4	2.508 ± 0.016	0.961 ± 0.004	1.244 ± 0.015	30.14 ± 0.07	31.11 ± 0.15	16.7 ± 1.1	V
1125	1.44	36.5	2.305 ± 0.039	0.928 ± 0.006	1.091 ± 0.039	29.77 ± 0.11	30.97 ± 0.23	15.6 ± 1.7	V
1146	4.91	53.0	2.415 ± 0.011	0.955 ± 0.004	1.172 ± 0.010	30.04 ± 0.05	31.10 ± 0.12	16.6 ± 0.9	V
1154	2.29	38.3	2.925 ± 0.001	1.094 ± 0.001	1.442 ± 0.001	30.38 ± 0.06	30.93 ± 0.08	15.3 ± 0.5	V
1158	3.07	42.1	2.746 ± 0.004	1.017 ± 0.002	1.256 ± 0.004	30.48 ± 0.11	31.18 ± 0.13	17.2 ± 1.0	V
1190	0.76	38.6	2.563 ± 0.014	1.003 ± 0.005	1.239 ± 0.014	30.10 ± 0.09	31.00 ± 0.16	15.8 ± 1.1	V
1226	15.51	98.0	2.863 ± 0.002	1.058 ± 0.001	1.369 ± 0.002	30.64 ± 0.07	31.21 ± 0.09	17.5 ± 0.7	V
1231	5.11	57.2	2.680 ± 0.004	1.027 ± 0.002	1.302 ± 0.004	30.33 ± 0.03	31.11 ± 0.07	16.7 ± 0.6	V
1242	3.61	55.7	2.322 ± 0.019	0.904 ± 0.009	1.118 ± 0.018	29.86 ± 0.05	31.05 ± 0.15	16.2 ± 1.1	V
1250	0.61	22.2	2.291 ± 0.013	0.904 ± 0.002	1.124 ± 0.013	29.93 ± 0.07	31.13 ± 0.14	16.9 ± 1.1	V
1253	3.66	54.0	2.841 ± 0.003	1.076 ± 0.002	1.368 ± 0.003	30.59 ± 0.08	31.20 ± 0.10	17.4 ± 0.8	V
1279	0.51	24.6	2.615 ± 0.003	1.014 ± 0.001	1.310 ± 0.003	30.32 ± 0.09	31.16 ± 0.10	17.1 ± 0.8	V
1303	1.31	37.2	2.560 ± 0.022	0.939 ± 0.006	1.217 ± 0.021	29.98 ± 0.05	30.88 ± 0.16	15.0 ± 1.1	V
1316	9.13	82.8	2.890 ± 0.001	1.091 ± 0.001	1.529 ± 0.000	30.61 ± 0.03	31.15 ± 0.04	17.0 ± 0.4	V
1318	1.52	33.9	2.438 ± 0.009	0.910 ± 0.003	1.140 ± 0.008	29.95 ± 0.04	30.98 ± 0.10	15.7 ± 0.7	V
1321	2.44	37.8	⋯	0.946 ± 0.003	1.171 ± 0.009	29.75 ± 0.05	30.80 ± 0.14	14.5 ± 0.9	V
1368	2.96	47.6	2.399 ± 0.018	0.936 ± 0.008	1.175 ± 0.017	29.80 ± 0.04	30.91 ± 0.15	15.2 ± 1.0	V
1412	1.07	38.7	2.845 ± 0.007	1.098 ± 0.002	1.350 ± 0.007	30.44 ± 0.05	31.08 ± 0.10	16.5 ± 0.8	V
1535	1.57	54.4	2.637 ± 0.005	1.021 ± 0.002	1.308 ± 0.005	30.50 ± 0.09	31.32 ± 0.12	18.4 ± 1.0	V

Table 2
(Continued)

VCC	Area (arcmin^2)	⟨Rad⟩ (arcsec)	$(u^* - z)$ (mag)	$(g - i)$ (mag)	$(g - z)$ (mag)	$\overline{m_i}$ (mag)	$(m - M)$[a] (mag)	D (Mpc)	Comment[b]
1537	2.70	44.3	2.403 ± 0.032	0.942 ± 0.009	1.154 ± 0.031	30.04 ± 0.08	31.16 ± 0.20	17.0 ± 1.6	V
1552	2.20	45.6	2.492 ± 0.007	0.965 ± 0.003	1.194 ± 0.007	29.93 ± 0.29	30.95 ± 0.31	15.5 ± 2.2	V
1588	0.50	47.7	2.133 ± 0.024	0.827 ± 0.006	1.018 ± 0.024	29.83 ± 0.03	31.22 ± 0.17	17.6 ± 1.4	V
1615	2.64	129.3	2.514 ± 0.024	0.911 ± 0.012	1.248 ± 0.023	30.37 ± 0.07	31.35 ± 0.18	18.6 ± 1.5	V
1619	2.06	40.7	2.291 ± 0.016	0.924 ± 0.007	1.104 ± 0.015	29.59 ± 0.06	30.82 ± 0.14	14.6 ± 1.0	V
1630	2.43	39.4	2.792 ± 0.008	1.086 ± 0.004	1.314 ± 0.008	30.45 ± 0.05	31.14 ± 0.11	16.9 ± 0.8	V
1632	4.07	51.3	2.822 ± 0.002	1.085 ± 0.001	1.383 ± 0.002	30.46 ± 0.08	31.11 ± 0.10	16.7 ± 0.7	V
1664	3.81	54.0	2.579 ± 0.012	0.981 ± 0.004	1.251 ± 0.012	30.19 ± 0.07	31.09 ± 0.14	16.6 ± 1.0	V
1692	3.20	61.5	2.345 ± 0.044	0.937 ± 0.012	1.204 ± 0.041	30.04 ± 0.07	31.18 ± 0.23	17.2 ± 1.8	V
1720	5.56	56.3	2.609 ± 0.008	0.970 ± 0.003	1.232 ± 0.008	30.28 ± 0.07	31.12 ± 0.12	16.8 ± 0.9	V
1727	1.24	114.7	2.457 ± 0.012	0.934 ± 0.005	1.221 ± 0.011	30.47 ± 0.09	31.52 ± 0.15	20.2 ± 1.4	V
1730	2.71	57.8	2.435 ± 0.018	0.936 ± 0.009	1.203 ± 0.017	30.14 ± 0.05	31.18 ± 0.15	17.2 ± 1.2	V
1813	7.66	74.8	2.705 ± 0.007	0.993 ± 0.003	1.256 ± 0.006	30.39 ± 0.09	31.13 ± 0.12	16.9 ± 1.0	V
1859	0.68	39.3	2.116 ± 0.021	0.791 ± 0.006	0.981 ± 0.021	29.59 ± 0.08	30.99 ± 0.17	15.8 ± 1.3	V
1869	1.76	54.7	2.832 ± 0.004	1.037 ± 0.001	1.297 ± 0.003	30.59 ± 0.08	31.19 ± 0.10	17.3 ± 0.8	V
1883	0.80	23.7	2.444 ± 0.002	0.953 ± 0.001	1.182 ± 0.002	30.15 ± 0.12	31.18 ± 0.13	17.3 ± 1.0	V
1903	2.63	49.3	2.759 ± 0.002	1.058 ± 0.001	1.353 ± 0.002	30.26 ± 0.04	30.97 ± 0.07	15.6 ± 0.5	V
1938	3.08	55.8	2.558 ± 0.019	0.937 ± 0.006	1.226 ± 0.019	30.21 ± 0.05	31.12 ± 0.15	16.8 ± 1.2	V
1978	3.04	47.2	2.964 ± 0.001	1.098 ± 0.000	1.427 ± 0.001	30.64 ± 0.07	31.11 ± 0.08	16.7 ± 0.6	V
1999	1.00	26.3	2.487 ± 0.007	0.934 ± 0.002	1.195 ± 0.007	30.07 ± 0.08	31.06 ± 0.12	16.3 ± 0.9	V
2000	3.57	55.1	2.242 ± 0.023	0.895 ± 0.007	1.060 ± 0.022	29.61 ± 0.04	30.88 ± 0.16	15.0 ± 1.1	V
2058	2.08	88.2	2.189 ± 0.027	0.863 ± 0.010	1.109 ± 0.026	29.91 ± 0.07	31.22 ± 0.19	17.5 ± 1.5	V
2066	1.65	63.0	1.986 ± 0.037	0.751 ± 0.017	0.911 ± 0.037	29.64 ± 0.07	31.20 ± 0.21	17.4 ± 1.7	V
2087	3.71	49.4	2.473 ± 0.015	0.944 ± 0.004	1.179 ± 0.014	30.21 ± 0.06	31.20 ± 0.14	17.4 ± 1.1	V
2092	3.67	55.0	⋯	1.053 ± 0.002	1.325 ± 0.007	30.26 ± 0.05	30.97 ± 0.13	15.6 ± 0.9	V
2095	2.63	53.3	⋯	0.874 ± 0.005	1.223 ± 0.015	30.02 ± 0.06	31.15 ± 0.18	17.0 ± 1.4	V

Notes.
[a] The preferred distance modulus is derived adopting the $\overline{M_i}$ versus $(u^* - z)$ calibration (Table 3) when u^*-band is available, otherwise it is derived from the two-color calibration $\overline{M_i}$ versus $(g - i)/(g - z)$ (Table 4).
[b] Labels used: V—Virgo cluster proper (A or B clouds); W′—Virgo W′ member or candidate; M or W—member of either the ∼ twice more distant M or W clouds.

the light from faint sources; the aperture corrections for these magnitudes were obtained from a number of isolated sources in each frame using a curve-of-growth analysis out to large radii (Cantiello et al. 2009, 2011b). The cutouts of the NGVS images used for the analysis are ≈5′ wide on each side; on such scales the PSF variation is small enough that the typical rms scatter is ∼0.01 mag for the aperture corrections.[9]

Once the catalog of sources had been derived, the next step was to fit the luminosity function of the sources, which was necessary in order to estimate the amount of contamination from unmasked faint sources in the residual frame. We fitted a source magnitude distribution to a model, including a combination of the GCLF and a power-law background galaxy luminosity function (examples are shown in Figure 1, discussed below). As noted above, bright stars and the most extended sources had been masked and were therefore not present in the catalog. At these high Galactic latitudes, the surface density of fainter stars is small compared the GCs in the vicinity of bright galaxies. The best fit to the combined GCLF and galaxy luminosity function was used to derive the background fluctuation correction term, P_r, as described in previous works (e.g., Tonry et al. 1990; Cantiello et al. 2005; Mei et al. 2005b).

To determine the SBF amplitudes, we measured the azimuthal average of the power spectrum $P(k)$ within circular annuli of the masked residual frame, and modeled $P(k)$ as the power spectrum of a template PSF convolved with the mask image, $E(k)$, plus another term representing the power spectrum of noise unconvolved with the PSF. For the PSF term, we used from 2 to 12 individual isolated bright point sources near the target galaxy in each residual frame, as well as model PSFs constructed with DAOPhot (Stetson 1987, 1990). Each PSF was normalized and used separately to estimate the total fluctuation amplitude P_0 via a robust minimization method (Press et al. 1992) as the multiplicative factor in the power spectrum representation $P(k) = P_0 \times E(k) + P_1$, where P_1 is the unconvolved "white noise" term. We averaged the values of P_0 determined from all the available PSF templates, rejecting any PSFs that gave poor fits to the power spectrum. Finally, the SBF amplitude P_f was found by subtracting the background contamination term from the power spectrum amplitude $P_f = P_0 - P_r$.

Figure 1 illustrates the basic steps involved in the SBF measurement for four example galaxies representing the quartiles of the B_T interval for the sample studied in this work. In each row of the figure, the panels show: the target galaxy image; residual frame at the same intensity stretch with sources unmasked; residual frame with a tighter stretch after masking detected sources; fitted background luminosity function model; power spectrum of the residual frame compared to the scaled PSF power spectrum. The upturn in the power spectrum at low wavenumber k occurs because of remaining large-scale features in the residual frames; the downturn at high k occurs because of a correlation by the sinc-like interpolation kernel during image

[9] For galaxies close to MegaPrime image tile edges, where the PSF or the image quality might be rapidly changing on spatially small scales, we limited our aperture corrections, PSF selection, and SBF analysis to the regions with the best image quality.

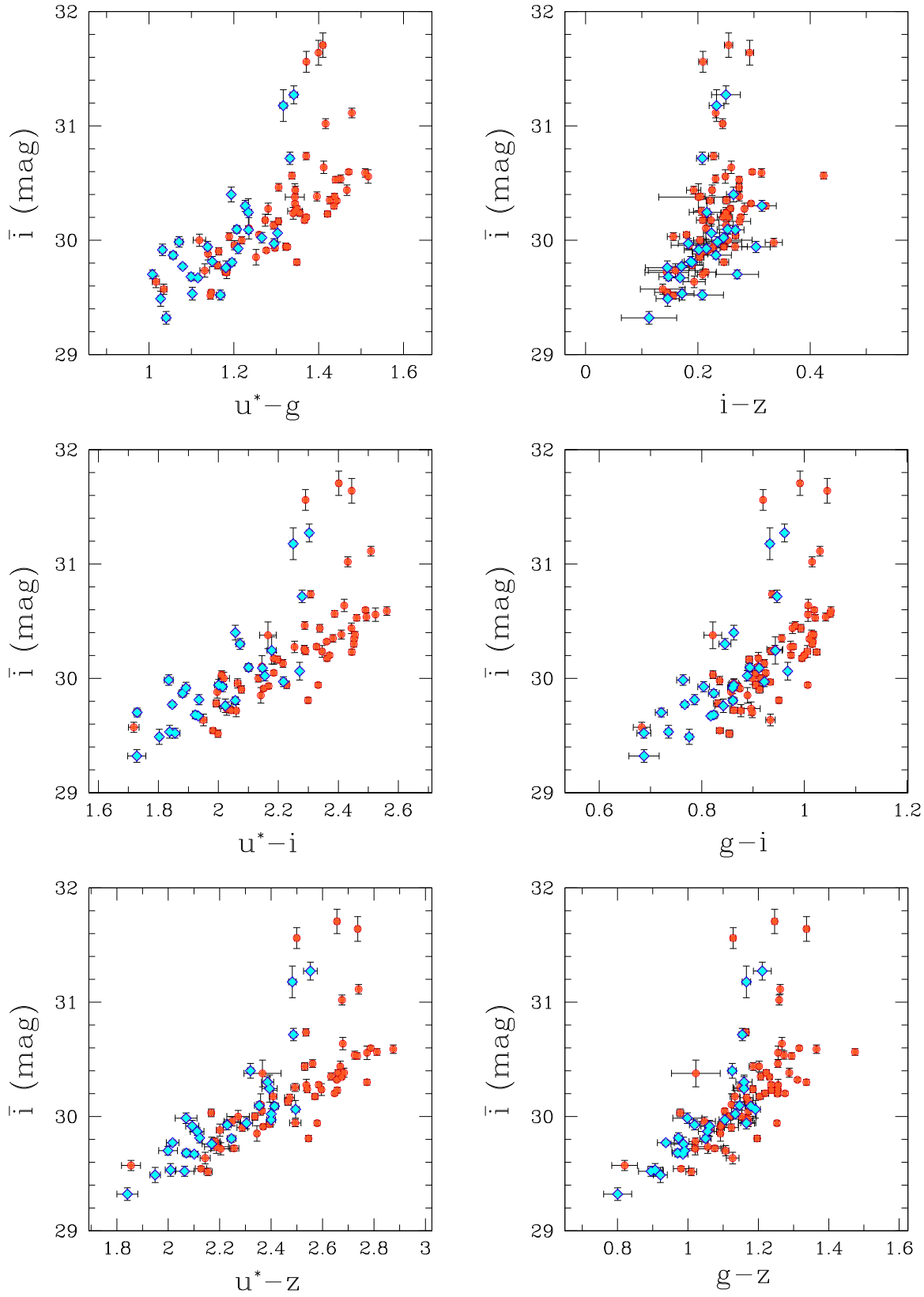

Figure 2. Measured SBF amplitudes vs. color. Red circles mark early-type galaxies, blue diamonds show late-type galaxies.

stacking (see Cantiello et al. 2005; Mei et al. 2005a). These high and low k ranges are excluded from the power spectrum fits. To define the best interval for the k wavenumbers, we examined the residuals of the observed power spectrum with respect to the model and rejected k-numbers where the residuals start deviating systematically from zero (e.g., Figure 7 in Cantiello et al. 2013). The exact k interval adopted for the fits depends on the size of the image used for the SBF analysis.

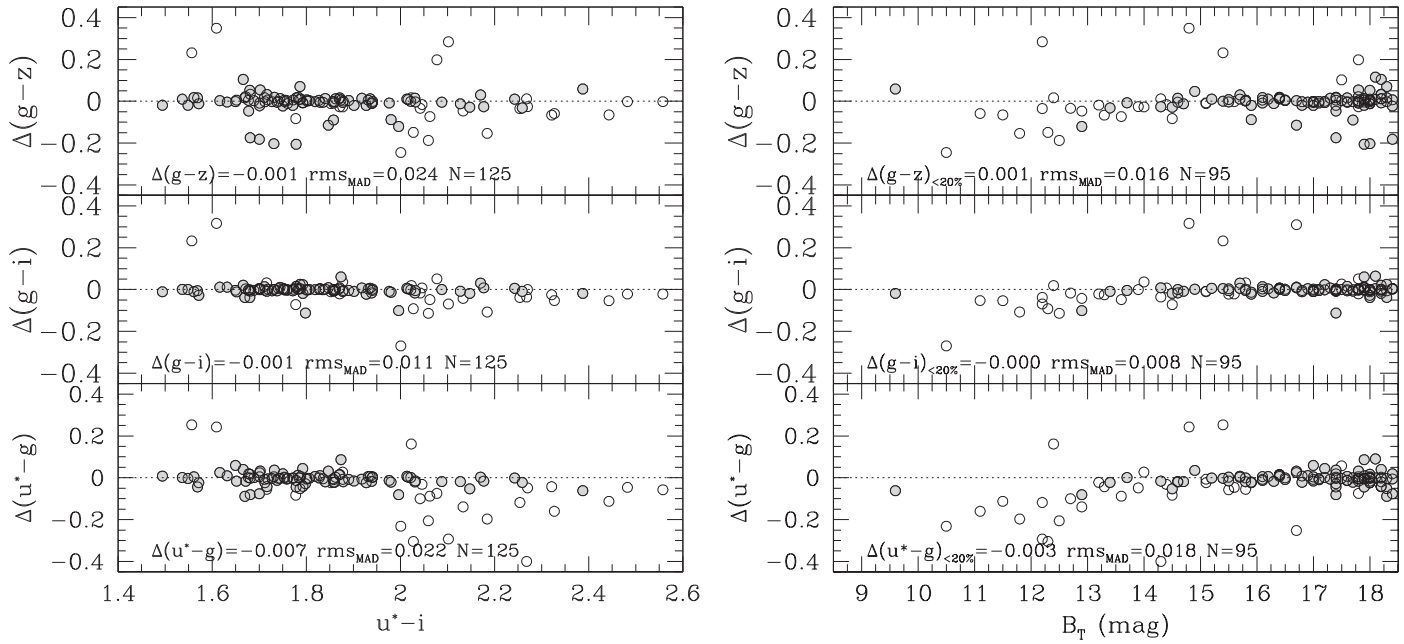

Figure 3. Left panels: color differences between the present work and Roediger et al. (2017, see the text). Filled dots refer to objects with SBF measurement radii within 20% of the effective radius adopted by Roediger et al. (2017). Right panels: as left, but vs. total magnitude B_T. The median difference $(\Delta(X–Y) = (X–Y)_{\text{this work}}–(X–Y)_{\text{Roediger+17}})$, rms, and the number of objects used for the full sample of common sources is reported in the left panels. The same quantities for the selected objects with SBF and R_e radii matching within 20%, are given in the right panels.

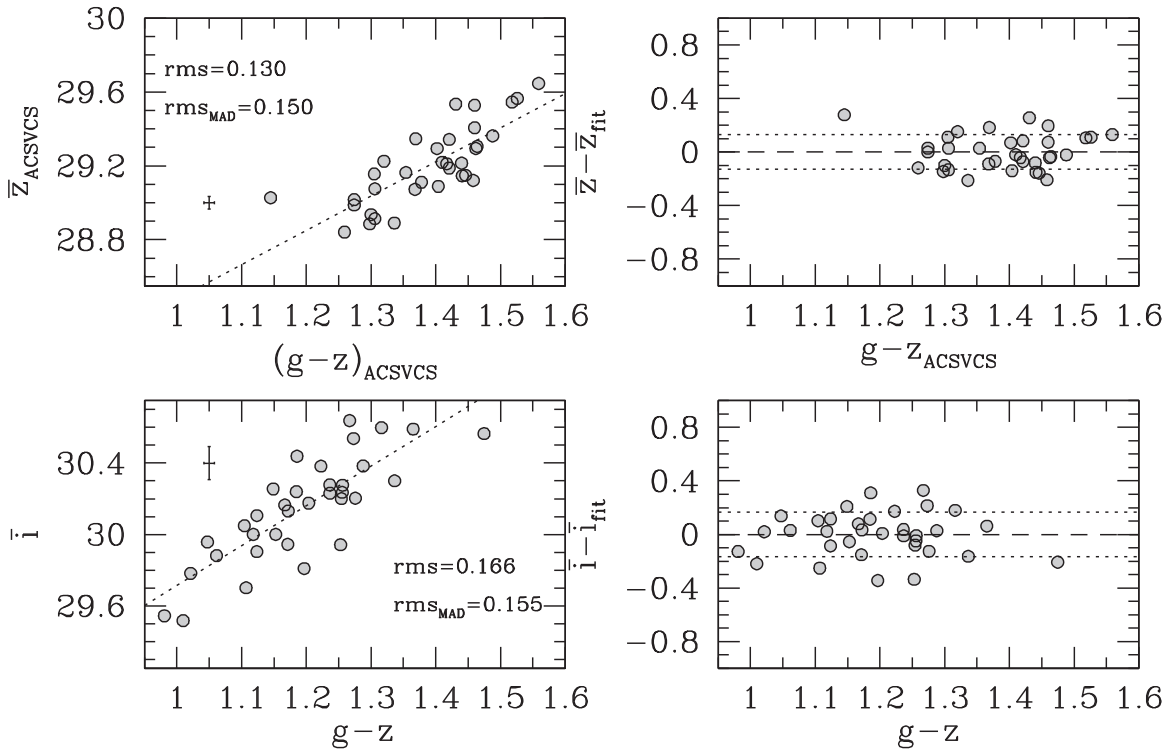

Figure 4. Left panels: measured SBF amplitudes vs. $(g - z)$ from the ACSVCS (z-band, upper panel) and from the present work (i-band, lower panel). The linear least squares fit to the data is reported with a dotted line. The rms scatter, and rms_{MAD} with respect to the linear fit are reported in each panel. The median error bars are also reported in the panels. Right: residuals with respect to the linear fit for the ACSVCS (upper panel) and the NGVS (lower). The dashed and dotted lines represent the zero and $\pm 1\sigma$ levels, respectively.

The second and third panels of each row in Figure 1 indicate the annuli used for the SBF measurements in the example galaxies. We also measure the integrated colors of the galaxies in the same annuli as used for the SBF measurements. Table 2 reports the area and the median radius of the annulus adopted for each galaxy in our sample, along with all possible unique color measurements and the SBF magnitude $\overline{m}_i$ derived within the annulus.[10] As explained in the following section, the table

[10] In order to derive the distance moduli $(m - M)$, the colors and magnitudes reported in Table 2, uncorrected for Galactic extinctions, were corrected using the values from Schlegel et al. (1998).

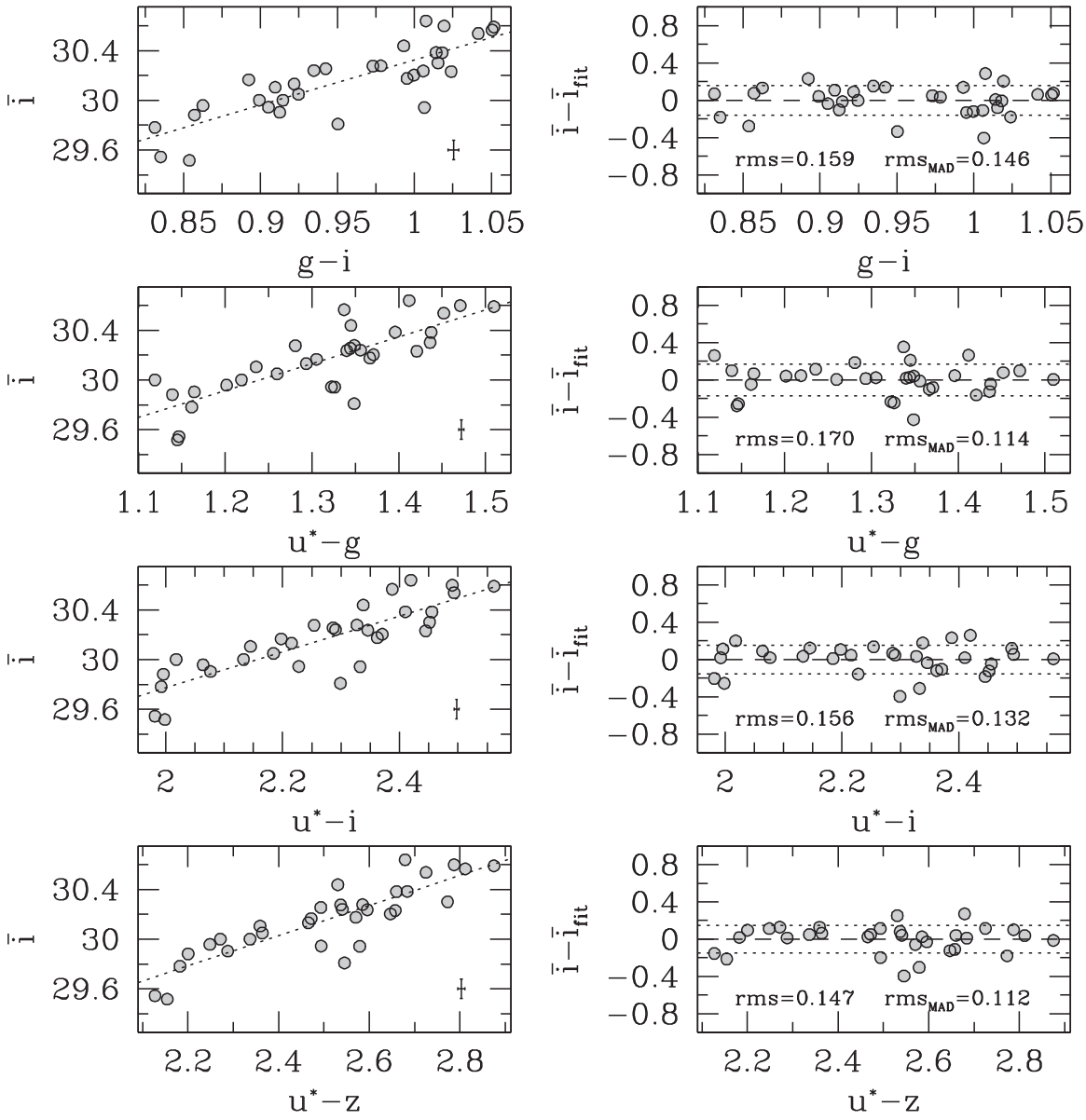

Figure 5. As in Figure 4, but for a selection of the other colors available from NGVS.

Table 3
Coefficients of the Fits $\overline{M}_i = \alpha + \beta \times$ [color − refcolor]

Color	α (mag)	β	Refcolor
$(g - i)$	-0.93 ± 0.04	3.25 ± 0.42	0.95
$(g - z)$	-0.90 ± 0.04	1.98 ± 0.16	1.20
$(u^* - i)$	-0.88 ± 0.04	1.27 ± 0.06	2.30
$(u^* - z)$	-0.93 ± 0.04	1.09 ± 0.04	2.50

also includes our preferred distance modulus for each galaxy and a comment about the likely subgroup membership inferred from the galaxy distance modulus. Figure 2 plots the apparent SBF magnitudes for the full sample of galaxies reported in Table 1 versus various integrated colors. In the panels of this figure, the early-type galaxies with morphological $T_{\rm type} < 0$ and late-type galaxies with $T_{\rm type} \geqslant 0$ are represented with red circles and blue diamonds, respectively.

4. Analysis

To derive distances from the SBF measurements, an accurate calibration of $\overline{M}_i$ is required. In this section, we analyze various options for the calibration and choose the optimum approach. The resulting distances for the 89 galaxies in our sample are presented in Section 5.

4.1. Calibrating SBF: Distances and Colors

The measured SBF magnitudes show a clear dependence on galaxy color that is recognizable even before applying any cluster-depth correction. Clearly, some data points in the plots are outliers with respect to the visual mean relations: this is in part due to the combination of the intrinsic depth of Virgo and the intrinsic scatter of the SBF method itself, but also to the presence of a sequence of objects offset by $\approx$+0.7 mag with respect to the most populated sequence on the $\overline{m}_i$ versus color diagrams, associated with the Virgo W′ group, and to a fraction of objects that are background

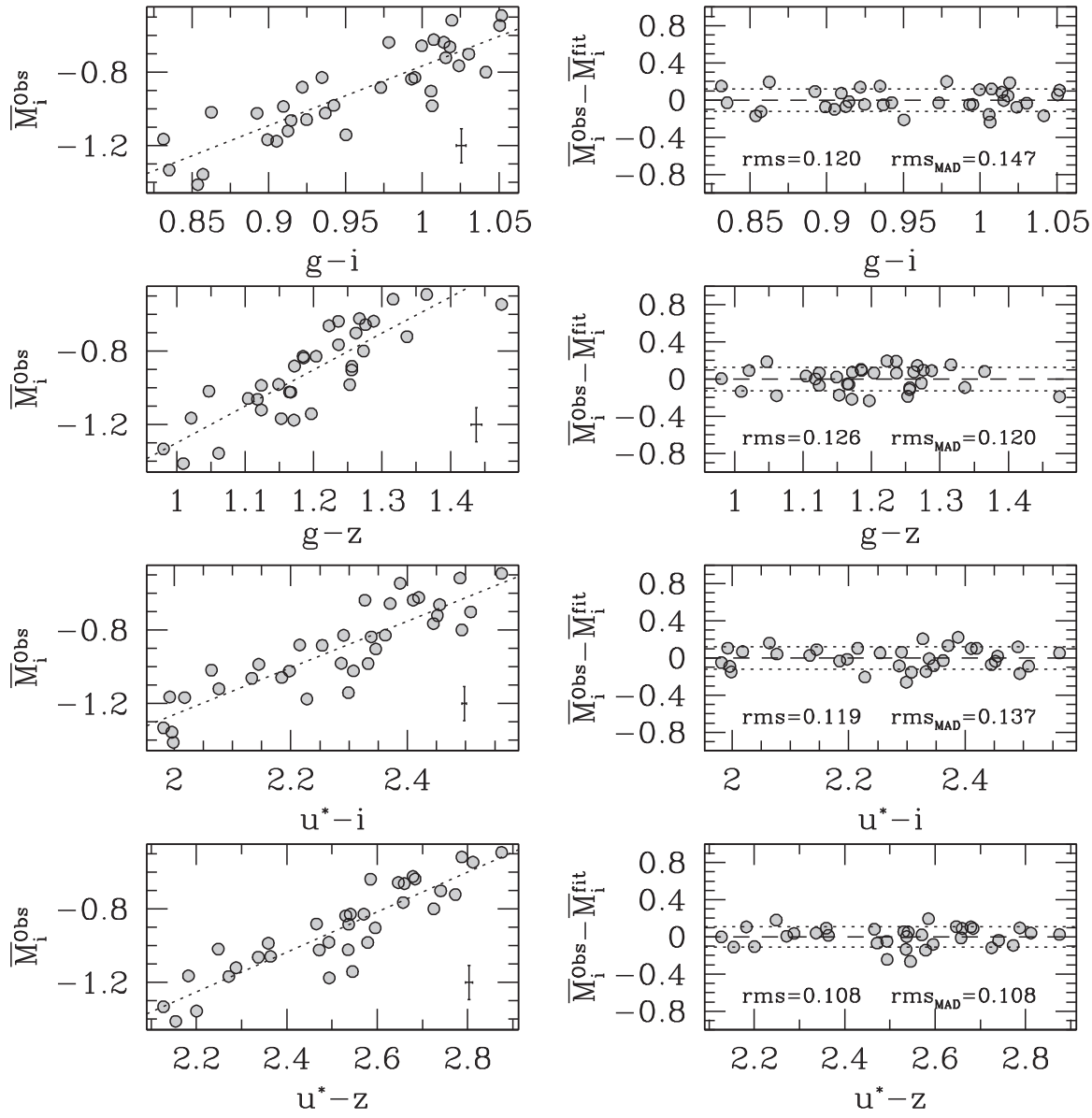

Figure 6. Left panels: absolute SBF magnitudes, $\overline{M}_i^{Obs}$, vs. color. The linear fit to data is shown with a dotted line; the median error bars include the uncertainty on the assumed distance modulus. Right panels: residuals with respect to the linear fit. The zero and $\pm 1\sigma$ lines are shown with dashed and dotted lines, respectively. The rms and $\mathrm{rms}_{\mathrm{MAD}}$ for each are reported in the right panels.

galaxies, possible members of the W and M subgroups (Sandage et al. 1985; Binggeli et al. 1987, 1993; Kim et al. 2014). To derive absolute $\overline{M}_i$ magnitudes, we adopt the ACSVCS distances listed in Table 1 for the 36 galaxies in common with our sample.

To verify our color measurements, we compared our results with the ones from Roediger et al. (2017), obtained from the same NGVS data used here. To increase the number of galaxies for the comparison, we extended the present data set to galaxies fainter than the limiting B_T adopted in this paper, and for which SBF analysis is in progress. Figure 3 shows the color difference (this work minus the results from Roediger et al. 2017) versus $(u^* - i)$ (left panels) and versus total magnitude B_T (right panels). Although based on the same data set, the statistical consistency of the measurements is not trivial, because the two studies adopt different analysis procedures, and the annular regions as well as the masking thresholds are different. The galaxies with the largest mismatch are the ones where the mean radius of the region inspected for SBF measurements differs substantially from the galaxy effective radius, R_e, adopted by Roediger et al. (2017) to determine colors. The comparison limited to the galaxies with $|(R_e - R_{\mathrm{SBF}})/R_{\mathrm{SBF}}| \leqslant 0.2$ (that is, the ones where the median radius of the region used for SBF and R_e differs by less than $\approx$20%) shows remarkable agreement, with Δcolor < 0.01 mag and root-mean-squared scatter rms $\lesssim 0.02$ mag.[11]

4.2. ACSVCS z-band SBF versus NGVS $\overline{m}_i$

A direct comparison of SBF magnitudes for the 36 galaxies in common between this work and the ACSVCS is indicative of the extra uncertainty of the present data set due to the lower spatial resolution of ground-based measures from CFHT/MegaCam data with respect to the space-based *HST*/ACS data.

[11] We also compared our colors with the measurements from Chen et al. (2010) based on SDSS data. The agreement is generally satisfactory for objects where the radius adopted for SBF analysis is similar to the annulus used for measuring colors.

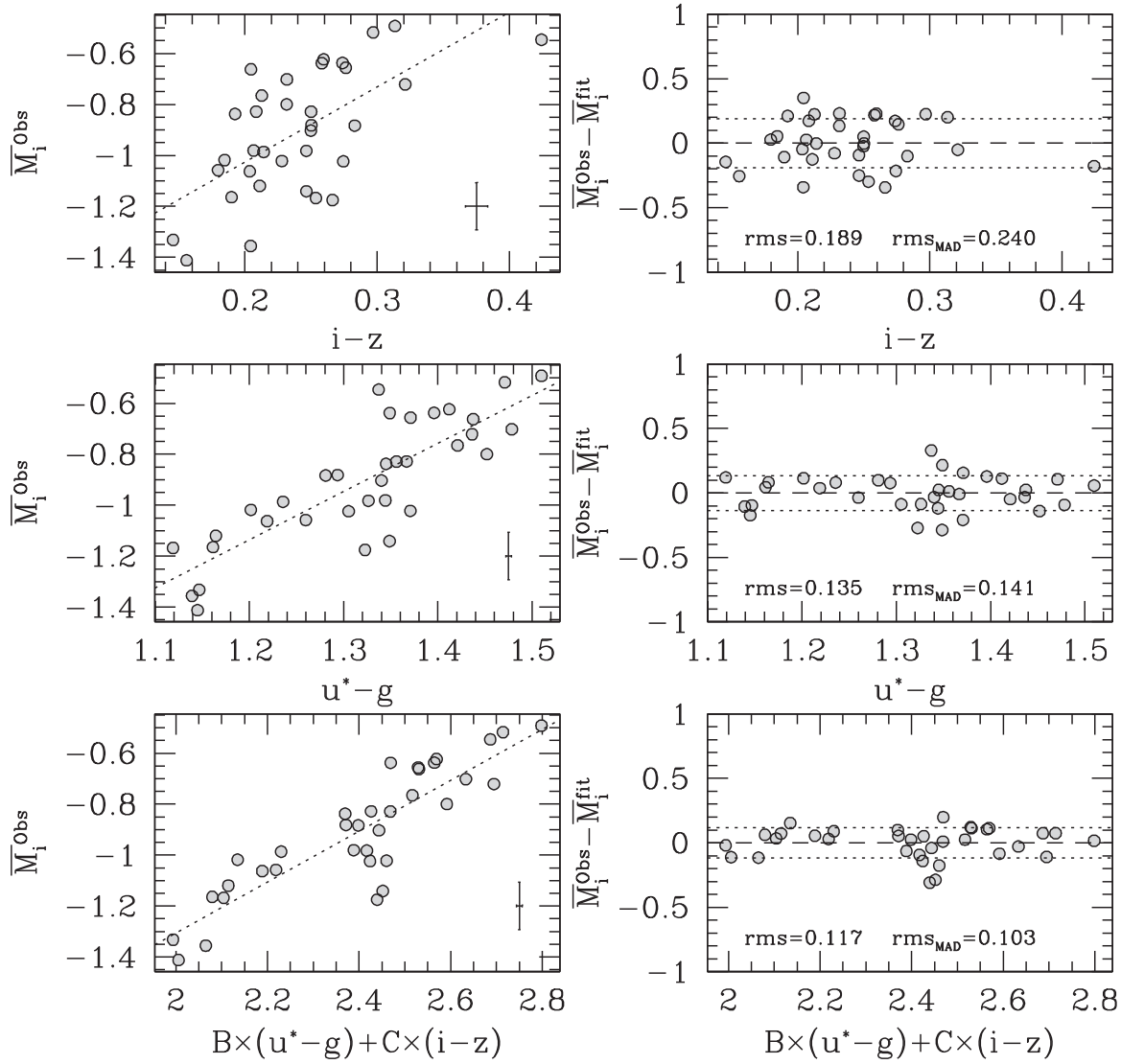

Figure 7. Upper and middle left panels: SBF vs. color relations for $(u^* - g)$ and $(i - z)$. The residuals with respect to the linear regression are shown in the right panels, using the same symbols as in Figure 6. The scatter of $(u^* - g)$ and $(i - z)$ color relations is sensibly larger than for the other colors, shown in Figure 6. Lower panels: two-color fit (left panel) and residuals (right) obtained by combining the $(u^* - g)$ and $(i - z)$. Note the lower scatter for the two-color with respect to the single-color relations.

Figure 4 shows the apparent SBF magnitude versus $(g - z)$ (left panels), and the residual with respect to a linear fit (right plots) for both the ACSVCS (upper panels) and NGVS measurements (lower panels).[12] The linear regressions, reported with the dotted line in the left panels of the figure, are obtained after rejecting from the sample the two galaxies in the W′ group (i.e., VCC 731 and VCC 1025). The rms reported in the figure shows that the set of measurements from the NGVS has ≈0.04 mag larger scatter than the ACSVCS. The scatter estimate $\mathrm{rms_{MAD}} \equiv 1.48 \times \mathrm{MAD}$, derived from the median absolute deviation (MAD[13]), is similar to the rms.

Figure 5 shows the apparent magnitudes $\overline{m}_i$ versus colors other than the $(g - z)$. For the sake of comparison, the two galaxies without currently available u-band magnitudes are not included in the plots. Together, Figures 4 and 5 show that, over the color interval of our bright galaxy sample, a linear relation is generally a good representation of the variation in SBF magnitude with color. However, even with the W′ galaxies omitted, depth effects within Virgo serve to increase the observed scatter in these relations (see Section 5). We therefore move on to fitting the calibrations in terms of absolute SBF magnitude.

4.3. Single-color Calibrations

For our first set of calibrations, we derive linear fits to the variation of the $\overline{M}_i$ values (derived from our $\overline{m}_i$ measurements and the ACSVCS distance moduli listed in Table 1) using a single NGVS color index as the independent variable. Since 2 of the 36 galaxies with ACSVCS distances lack u^* data, we therefore use 34 galaxies for these fits (including here the somewhat more distant W′ members). These single-color fits

[12] The ACSVCS team used a more refined calibration scheme than the simple linear scheme used here. However, the ACSVCS sample covered a wider color range, $0.8 \leqslant (g - z)_{ACS} \leqslant 1.6$ mag. Within the narrower color interval of the present work, the proximity to a linear relation increases, as the bend of the $\overline{M}_z$ calibrations by Mei et al. (2007) and B09 appears close to $(g - z)_{ACS} \approx 1.3$ mag.

[13] The median absolute deviation, defined as $\mathrm{MAD} = \mathrm{median}|X_i - \mathrm{median}(X)|$, is equal to the standard deviation for a Gaussian distribution, but is more robust than the standard deviation as it is less sensitive to outliers.

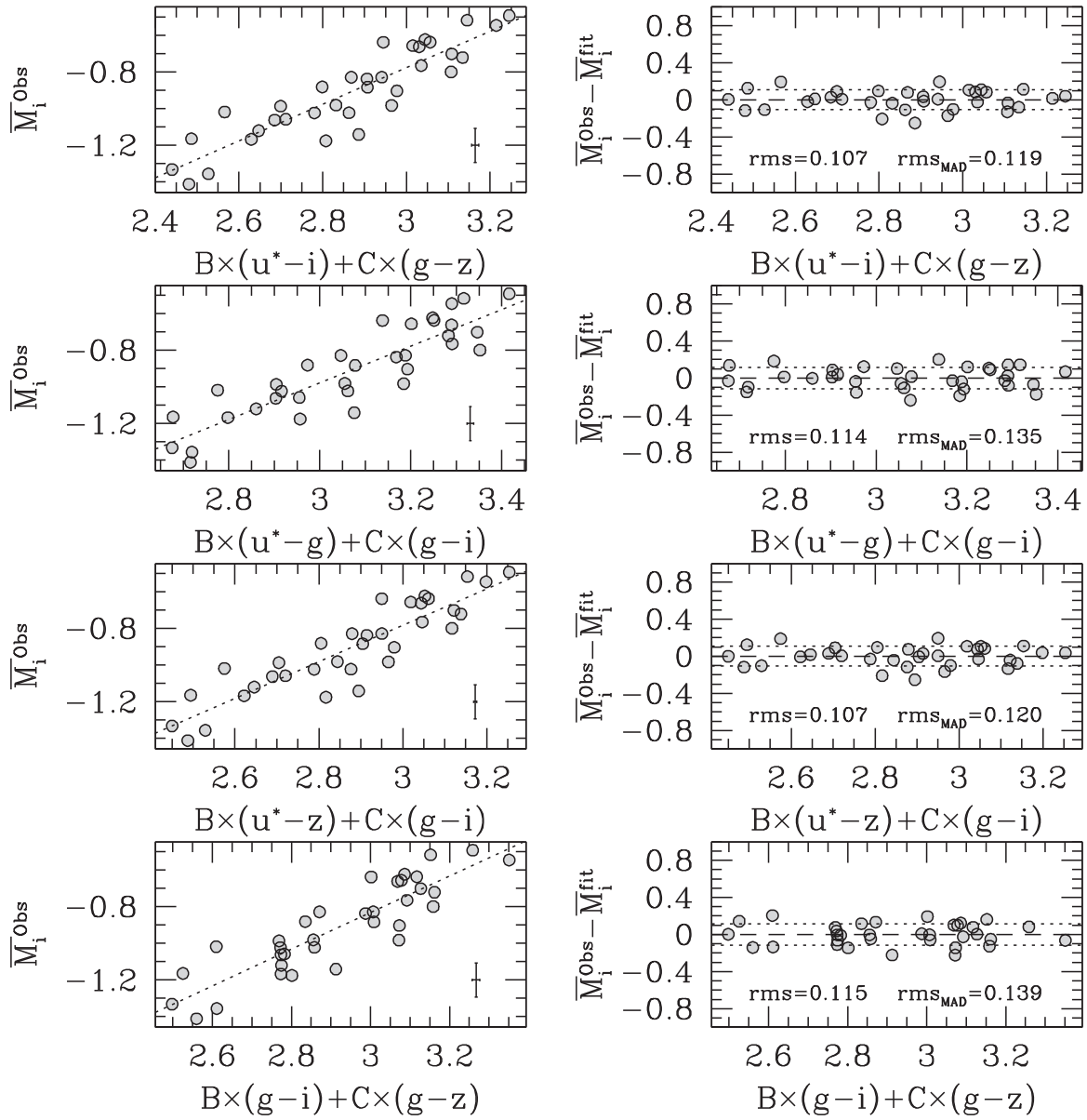

Figure 8. Two-color calibrations for various color combinations. Left/Right panels show the data used for the fits and the residual with respect to the latter.

are parameterized as

$$\overline{M_i} = \alpha + \beta \times [\text{color} - \text{refcolor}]. \quad (1)$$

The fitted α and β parameters, as well as the adopted "reference color" (refcolor), are given in Table 3 for four different color indices.

The four single-color linear fits are shown in Figure 6. The left panels plot the absolute SBF magnitude versus measured color along with the linear fit to the data (dotted lines); the right panels show the residuals with respect to the fits and the measured scatter values. Over the color range of the galaxies in this sample, the fit of $\overline{M_i}$ versus $(u^* - z)$ (bottom panels in Figure 6) exhibits the lowest scatter, with rms $\approx$ 0.11 mag.

4.4. Dual-color Calibrations

SBF calibrations based on multiple color indices can potentially provide improved characterization of the dependence of $\overline{M_i}$ on stellar population properties. This would manifest as a lower scatter in the empirically derived SBF calibrations. For example, Figure 7 shows one case where the combination of two-color indices, $(u^* - g)$ and $(i - z)$, gives a lower calibration scatter than either of the colors individually (single-color fits and residuals are shown in the upper and middle panels; the lower panels show the dual-color relation). However, because of their narrow wavelength baselines, neither $(u^* - g)$ nor $(i - z)$ are preferred choices for the

Table 4
Coefficients of the Fits $\overline{M_i} = A + B \times \text{color}_1 + C \times \text{color}_2$

Color$_1$	Color$_2$	A (mag)	B	C
$(u^* - i)$	$(g - z)$	−3.78	+0.77	+0.94
$(u^* - g)$	$(g - i)$	−3.98	+0.71	+2.22
$(u^* - z)$	$(g - i)$	−3.78	+0.86	+0.75
$(g - i)$	$(g - z)$	−3.83	+1.98	+0.86

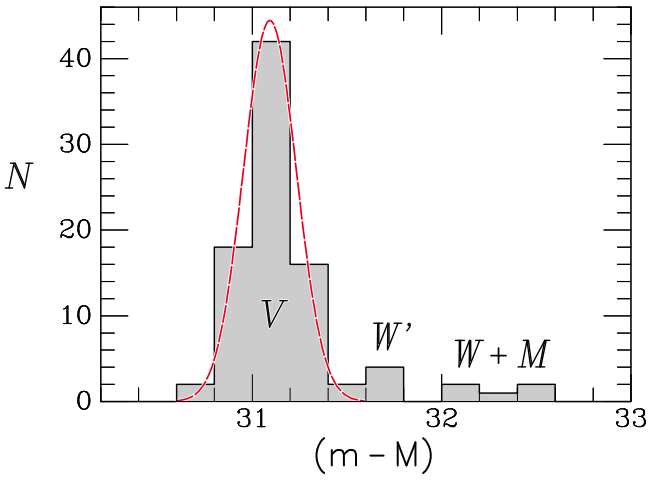

Figure 9. Histogram of distance moduli presented in Table 2. The loci of the main Virgo cluster (V in the plot), the W′ group, and the W and M clouds are indicated. For comparison, the red dashed curve shows a Gaussian of mean = 31.09 mag and $\sigma = 0.14$ mag, which provides a reasonable representation of the peak corresponding to the main Virgo cluster. Note that 0.14 mag is both the rms dispersion that we measure and the median estimated error; thus the width of the V peak is mainly due to measurement error.

single-color calibration. Thus, this case is simply an illustration of the concept.

Using the available NGVS color data, we derived fits of $\overline{M}_i$ to combinations of two different color indices in the following form:

$$\overline{M}_i = A + B \times \text{color}_1 + C \times \text{color}_2. \quad (2)$$

The fitted values of A, B, and C for four different choices of color_1 and color_2 are given in Table 4. Figure 8 shows the four dual-color fits and their residuals.

In general, by comparing the $\overline{M}_i$ calibrations based on a single color with the calibrations based on a combination of two colors, we find that even the widest two-color combinations result in a calibration scatter for $\overline{M}_i$ comparable to the single-color $(u^* - z)$ calibration. That is to say, for the present magnitude-limited sample, we do not find strong evidence in favor of the two-color option with respect to the more standard one-color $\overline{M}_i$ calibration, as long as the calibrating color involves the u^* band.

Nevertheless, for the forthcoming larger set of NGVS SBF measurements, extending to fainter galaxies that tend to be bluer than the color range explored in the current sample, the two-color calibrations confer some benefits over the traditional single-color option. For instance, using a single-color index for the calibration, B09 showed that the scatter increased at the bluest colors; models suggest that this scatter may be reduced with a second color, although this remains to be confirmed empirically. Moreover, the simple linear approximation to the SBF–color relation is no longer valid at such blue colors (Mei et al. 2005b, B09); thus, the calibration will need to be revisited for the extended sample in any case.

5. Results

5.1. SBF Distances for Bright Galaxies in the NGVS

We now apply the color calibrations described in the previous sections to derive the distance to each galaxy in our sample. We select the $\overline{M}_i$ versus $(u^* - z)$ relation as our preferred calibration because it has the lowest rms scatter of all the single-color calibrations, and adding a second color such as $(g - i)$ does not further reduce the scatter. For the six galaxies where no u^*-band magnitudes are available, we adopt the calibration of $\overline{M}_i$ based on the $(g - i)/(g - z)$ color combination, as it has smaller scatter than either of the two single-color options that do not include the u^* band.

Adopting these calibrations, we derive the distances reported in Table 2 for the 89 galaxies in the present sample. We point out a few noteworthy results:

1. We find that VCC 0049 (NGC 4168), which has been classified as a likely member of the M cloud (Ftaclas et al. 1984; Binggeli et al. 1993), is at a distance $d = 31.4 \pm 1.9$ Mpc ($m - M \approx 32.5$ mag), nearly twice as far as the main body of the Virgo cluster.
2. The four galaxies VCC 0220, VCC 0222, VCC 0341, and VCC 0345, classified by Binggeli et al. (1993) as members of the W cloud, are all significantly behind the main Virgo cluster and have a mean d of 28.7 ± 1.1 Mpc. Their mean heliocentric velocity is 2120 km s^{-1} with a dispersion of ≈200 km s^{-1}. The brightest of these is VCC 0345, or NGC 4261, which is also the only morphologically classified giant elliptical; we take it to be the brightest group galaxy (BGG).
3. As also found by the ACSVCS papers, VCC 0731 (NGC 4365) and VCC 1025 (NGC 4434) are members of the Virgo W′ group at $m - M \approx 31.75$ ($d \approx 22.5$ Mpc). In addition, we find VCC 0648 and VCC 0657 are likely W′ group members based on their distances, velocities, and small angular separations (1.2 deg and 0.3 deg, respectively) from NGC 4365, the W′ BGG.
4. VCC 0199 (NGC 4224) has an estimated $d = 21.5 \pm 1.3$ Mpc, which is consistent with being a member of the W′ group. However, its velocity of 2584 km s^{-1} is much more similar to the mean for the W cloud galaxies, as compared to the typical $v \approx 1200$ km s^{-1} of the W′ members (Figure 10, right panel). Its angular position is somewhat closer to the mean W cloud position, but because W is ≈25% more distant than W′, its physical separation would be smaller from NGC 4365 if it were at the mean d of the W′ group than it would be from NGC 4261 if it were at the d of the W cloud. We suggest that VCC 0199 may be a high-velocity member of the W′ group. However, because it is a spiral with significant dust, our confidence in the SBF distance is much weaker than if it were an elliptical galaxy, and we consider the membership assignment uncertain.
5. The remaining galaxies, marked with "V" in Table 2, have a mean $\langle m - M \rangle = 31.090 \pm 0.013$ mag, or $d = 16.5 \pm 0.1$ Mpc, which is the same mean Virgo distance from B09 quoted above. This is not entirely trivial, since only 43% (34 of 79) of the V sample was in the ACSVCS. Our median estimated measurement error is 0.14 mag; thus, the dispersion in the distance moduli for the V sample mainly reflects measurement error.
6. We derive the intrinsic dispersion in distance modulus for the galaxies in the V sample, $\sigma_{\rm Vir}$, used for deriving the cluster depth, as follows. If we call the total observed scatters in Figure 5 (labeled "rms" in the figure) $\sigma_{\bar{i}-\bar{fit}}$, which include the depth effect, and the scatters in Figure 6

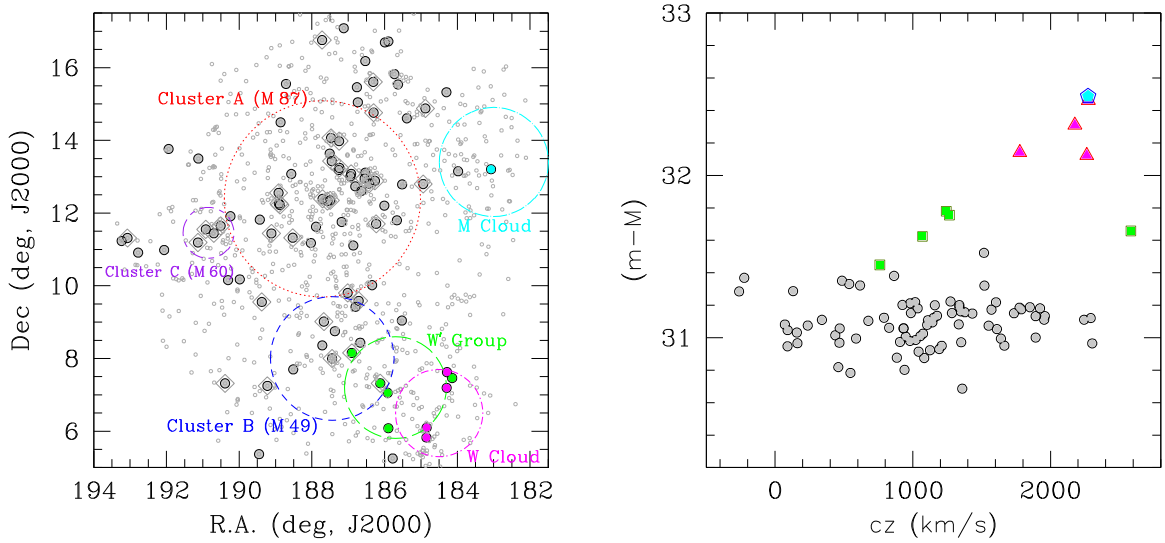

Figure 10. Left: map of the sky positions of the 89 galaxies in our sample, shown with large filled symbols. Small empty dots plot all possible and confirmed VCC members brighter than $B_T \approx 18$ mag. The 36 galaxies also in the ACSVCS are marked with gray diamonds. The substructures discussed in the text are identified by large symbols of various colors, using the locations and radii from Boselli et al. (2014, see the text). Note that these circles provide only rough indications of the structures; for instance, only the centermost galaxy in the "M" circle is at the distance of the M cloud, while we identify a total of nine galaxies as belonging to either W or W′ based on their distances. The possible members of the W′ group and of the W and M clouds are also identified using the same color coding of the respective circles. Right: *Hubble* diagram for the 89 galaxies in our sample. Symbol and color coding is the same as in the left panel.

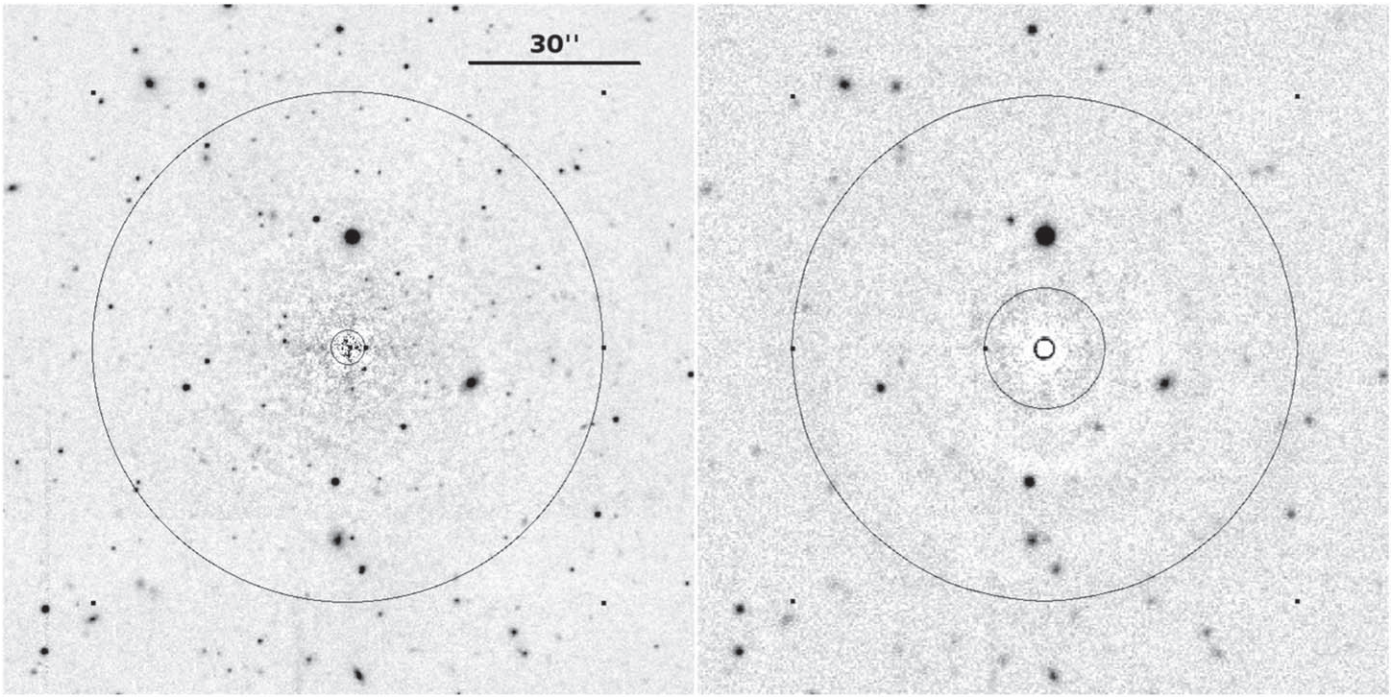

Figure 11. Left: NGVS *i*-band residual image of VCC 0648 (NGC 4339). Right panel: *I*-band image of the same galaxy from the SBF survey of Tonry et al. (1997, 2001), obtained with the 2.4 m Hiltner telescope at MDM Observatory in 1992. In both panels, the thin solid circles show the inner and outer radii of the annular region adopted to measure the amplitude of fluctuations.

$\sigma_{\overline{M_i}-fit}$, which do not contain the galaxy distance, then:

$$\sigma_{\rm Vir} = \sqrt{\sigma^2_{\overline{i}-fit} - \sigma^2_{\overline{M_i}-fit} - \sigma^2_{m-M}}$$

where σ_{m-M} is the median error in the assumed distance modulus, ∼0.07 mag for the ACSVCS distance moduli (Table 1).

Using the rms values for the $(u^* - z)$ calibration, we obtain $\sigma_{\rm Vir} \sim 0.07$ mag, or $\sigma(d_{\rm Vir}) \sim 0.55$ Mpc. The mean calculated from the four calibrations reported in Figures 4–6 is $\sigma(d_{\rm Vir}) = 0.6 \pm 0.1$ Mpc, corresponding to a $\pm 2\sigma$ depth of 2.4 ± 0.4 Mpc, a result consistent with Mei et al. (2007).

7. The V sample includes VCC 1727 (NGC 4579/M 58) with $(m - M) = 31.52 \pm 0.15$ mag. This is the only putative V galaxy with $(m - M) > 31.4$ mag; given its center-east location projected within the A subcluster, it is not a candidate W′ member. VCC 1727 is a spiral, and these tend

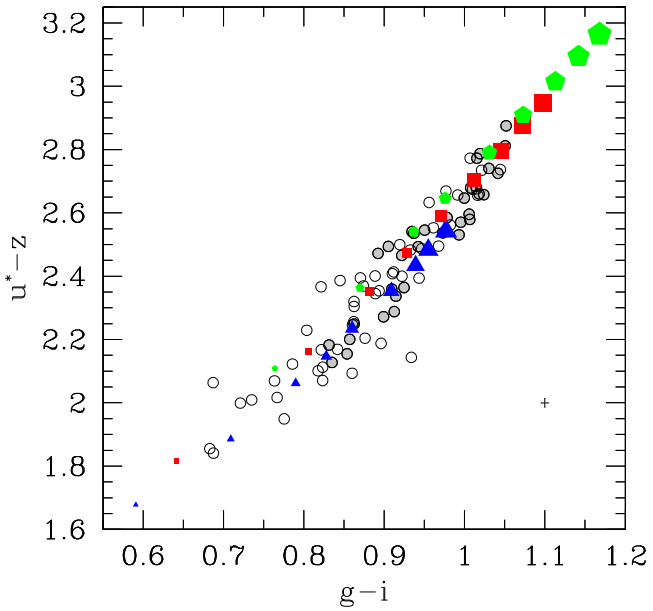

Figure 12. Color–color diagram of NGVS galaxies presented in this work, compared to SPoT stellar population models. Empty circles mark the full sample of SBF galaxies, gray-filled circles mark the galaxies in common with the ACSVCS. The median errors are shown as a cross on the lower right side of the panel. SSP models for [Fe/H] = −0.35, 0.0, and +0.4 are marked with blue triangles, red squares, and green pentagons, respectively. The age range plotted is 1–14 Gyr (1, 2, 3, 4, 6, 8, 10, 12, and 14 Gyr) with increasing symbol size for older ages.

to be either in front of, or behind, the Virgo core (e.g., Kelson et al. 2000). In any case, the weighted mean V distance modulus is unchanged if this galaxy is excluded.

Figure 9 presents a histogram of the distance moduli given in Table 2. The bins spanning Virgo proper, the W′ group, and the W and M clouds are indicated. The distribution of the galaxies on the sky is shown in Figure 10 (left panel). In the figure, the 89 galaxies in our sample and the 36 targets in common with the ACSVCS are indicated with filled symbols and gray empty diamonds, respectively. We also plot all possible and confirmed VCC members brighter than $B_T \approx 18.0$ mag, from Binggeli et al. (1985). Some of the substructures in Virgo, i.e., the A, B, and C clusters (centered on M 87 M 49, and M 60 respectively), the W′ group, and the W and M clouds are also indicated using circles of different colors and line-type adopting the positions and radii given in Boselli et al. (2014).[14] With the present data set, we find no significant difference in the mean distances of the galaxies within the A, B, and C subclusters. To further highlight the presence of substructures, also shown in Figure 9, we plot the *Hubble* diagram of the 89 galaxies in our sample in the right panel of Figure 10.

The results do not change substantially when the two-color calibration based on $(g - i)$ and $(g - z)$ is used instead of our preferred $(u^* - z)$ calibration for all galaxies, rather than only for the six galaxies currently lacking u^* data. The mean distance modulus of Virgo, after excluding W′, W, and M galaxies, is virtually unchanged. Moreover, for VCC 0657, one of the new W′ candidates, we find $m - M = 31.70 \pm 0.37$, which is consistent with the adopted value of 31.45 ± 0.31 mag, but closer to the W′ mean of ≈31.75 mag.

5.2. Comparisons with the Literature and Models

We compared our distance results to those of other studies; apart from our calibrating ACSVCS sample, the main overlap is with the Torny et al. (2001, hereafter Ton01) ground-based *I*-band SBF survey. The present and Ton01 samples have 31 galaxies in common. The distances agree well on average, with $(m - M)_{\rm NGVS} - (m - M)_{\rm Ton01} = -0.02 \pm 0.05$ mag and an rms of 0.29 mag.[15] The rms is reduced to ≈0.23 mag when the three most deviant galaxies are excluded from the comparison. After rejecting the three outliers (discussed below), the reduced χ^2 of the differences for the remaining 28 galaxies is $\chi^2_\nu = 1.18$. The three largest outliers in the comparison to Ton01 are VCC 0648, VCC 0958, and VCC 1938 (NGC 4339, NGC 4419, and NGC 4638, respectively). We discuss each of these in turn.

Our distance modulus for VCC 0648/NGC 4339 is ≈0.65 ± 0.20 mag larger (≈1.9 times more distant) than Ton01, or more than 3σ. The Ton01 quality flags for the galaxy are below average. Figure 11 compares the NGVS *i*-band and Ton01 *I*-band (J. Tonry 2018, private communication) images of the galaxy-subtracted frame used for the respective SBF measurements. In the left panel, we show the NGVS image, which reveals a large number of sources, not visible in the image used by Ton01 (right panel), many of which are likely GCs in VCC 0648. The main difference between the images is the seeing: the older data have a PSF FWHM of ≈1.″25, while our NGVS image has FWHM ≈0.″55. The poorer seeing of the older data apparently caused, in this particular case, a poor characterization of the GCLF because the data do not reach the turnover magnitude. As pointed out in Ton01 and other works, this can lead to an underestimated P_r correction, resulting in an overestimated fluctuation amplitude and an artificially low distance modulus. In the case of the much deeper NGVS image, we see the turnover in the GCLF. We conclude that our distance is much more reliable and, as discussed above, this galaxy is a newly recognized member of the W′ group.

For VCC 0958/NGC 4419, Ton01 reported $(m - M) = 30.65 \pm 0.25$ mag, which places it in front of Virgo with a significance of 1.8σ. The Ton01 quality flags are quite poor, as is also indicated by the relatively large quoted error. We find $(m - M) = 31.29 \pm 0.18$ mag, based on the $(u^* - z)$ calibration. Using the two-color $(g - i)/(g - z)$ calibration, we derive $(m - M) = 31.13 \pm 0.27$, which is consistent with the $(u^* - z)$-calibrated distance, and closer to the Virgo mean. The Ton01 seeing for this galaxy was a relatively good 0.″85, but it is a highly inclined spiral with significant dust, and therefore more difficult for the SBF method. Other recent distance estimates to the galaxy include $(m - M) = 31.06 \pm 0.25$ from the TF luminosity–linewidth relation by Gavazzi et al. (1999, revised to a mean Virgo distance modulus of $m - M = 31.09$), and $(m - M) = 31.24$ from SNe Ia (Reindl et al. 2005). This SNe Ia distance modulus is based on the peculiar supernova SN1984A and $H_0 = 60\,{\rm km\,s^{-1}\,Mpc^{-1}}$; assuming $H_0 = 70\,{\rm km\,s^{-1}\,Mpc^{-1}}$ the distance modulus becomes $(m - M) = 30.91$ mag. The "expected random error" reported by Reindl

[14] With respect to Boselli et al. (2014), we have slightly changed the location of the circles representing the W cloud and the W′ group loci, as well as their radii, to better match the location of the galaxies.

[15] The Ton01 distances have been revised using Equation (A1) from Blakeslee et al. (2010) to correct for a small residual bias in Ton01 distances for galaxies with the lowest SBF measurement quality.

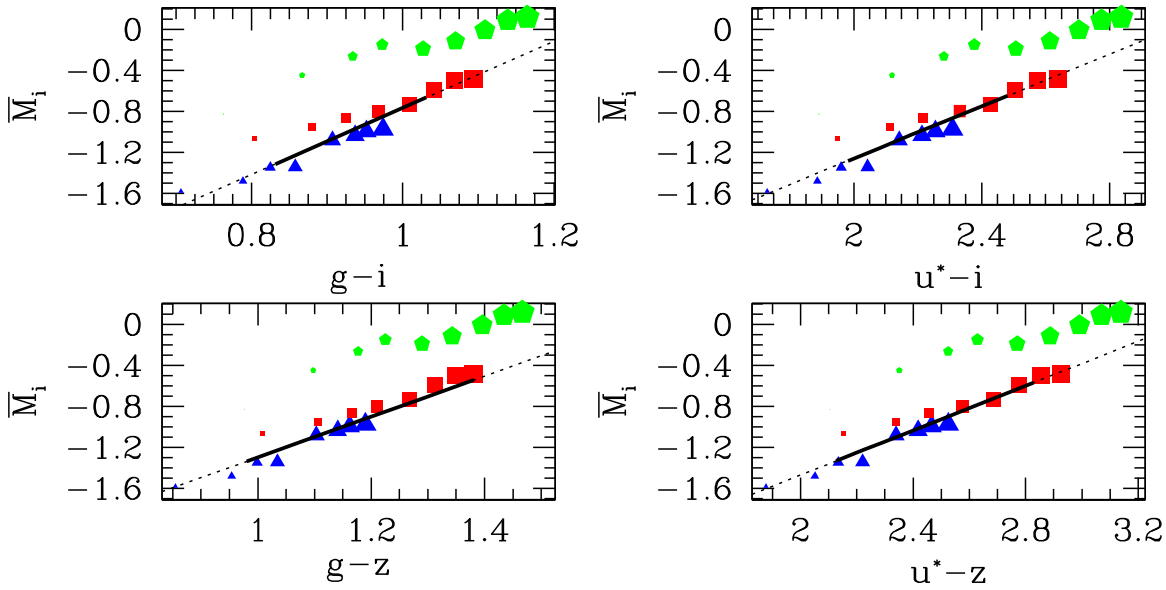

Figure 13. SBF vs. color calibrations: comparison of empirical relations and models. Symbols for models are the same as those in Figure 12. In each panel, the linear fit to the SBF vs. color relation is marked with a black dotted line. The thick solid black line refers to the color interval of the objects used for deriving the empirical relation.

et al. (2005) is $\sigma_{m-M} = 0.14$ mag, although the distance moduli for single objects could be less accurate. In summary, while the SNe Ia distances are not conclusive, based on our and TF distances VCC 0958 appears to be close to the mean distance of Virgo.

For VCC 1938/NGC 4638, we find $(m - M) = 31.12 \pm 0.15$ mag, whereas Ton01 reported $(m - M) = 31.68 \pm 0.26$ mag, which differs by 1.9σ. As shown in Table 1, this galaxy also has a measured ACSVCS distance modulus of 31.19 ± 0.07 mag, which agrees with our value. Note that the zero points of all three of these surveys are linked, but the individual distances are independent. Given our agreement with the much higher quality ACSVCS distance, we again conclude that our measurement is likely accurate.

Finally, we have also done preliminary comparisons of our measured SBF–color and color–color relations to predictions from the Teramo-SPoT simple stellar population (SSP) models (Cantiello et al. 2003; Raimondo et al. 2005; Raimondo 2009).[16] The comparison in Figure 12 indicates that the range of observed colors corresponds with the color sequence expected from the SSP models in the metallicity and age ranges $-0.35 \leqslant$ [Fe/H] $\leqslant +0.4$ dex, $1 \leqslant t \leqslant 14$ Gyr. It is worth noting that the galaxies do not extend to the region of the plot with the highest [Fe/H] values and oldest ages.

The four panels of Figure 13 compare the linear fits reported in Table 3 to SSP model predictions. In the figure, the thick black lines represent the empirical fits and only extend over the range of colors used in deriving them; dotted lines indicate linear extrapolations to the fits. The matching between fitted relations and models with [Fe/H] between −0.35 dex and solar (blue triangles and red squares in the figure), for ages older than ≈5 Gyr, is quite good. The super-solar metallicity models (green pentagons) predict fainter SBF magnitudes at the observed colors. This appears to indicate that our SBF measurements are done in regions of the galaxy with mean metallicity near solar, although it is also true that the later stages of stellar evolution are less well constrained at such high metallicities. Very similar results from model comparisons with ACS I_{814} SBF data were reported by Blakeslee et al. (2010), and from spectroscopic analyses by Trager et al. (2000) and Terlevich & Forbes (2002).

[16] Models in *UBVRIJHK* are available at http://www.oa-teramo.inaf.it/spot. The new models used here, for SDSS and MegaCam photometric system, will be tabulated in the next paper of this series.

6. Summary and Conclusions

We have presented the first SBF measurements using the panoramic, multiband imaging data from the NGVS survey. We described the procedures for SBF analysis of the *i*-band data, and presented multiple calibrations of the SBF absolute magnitude $\overline{M_i}$ in terms of individual color indices and combinations of two different indices, the so-called "single-color" and "two-color" calibrations. By comparing the measured scatter in the relations, we chose, as our preferred calibration, the relation between $\overline{M_i}$ and $(u^* - z)$ color. For the range of colors covered by the present data set, we find that additional information from the $(g - i)$ color measurements do not significantly improve the rms scatter in the calibration. For a small number of galaxies that do not currently have u^* data, we instead used an alternate dual-color calibration involving both $(g - i)$ and $(g - z)$. The observed scatter in both of these calibrations is ≈0.11 mag, or about 5% in distance, including both measurement error and intrinsic scatter from stellar population effects.

In all, we have reported SBF distances for 89 galaxies brighter than $B_T \approx 13$ mag, the majority of which have had no previous SBF measurements. The NGVS observation strategy was optimized for accurate SBF measurements to galaxies at the mean distance of the Virgo cluster, ≈16.5 Mpc, but the superb image quality of NGVS enables high-quality SBF measurements out to $d > 30$ Mpc. For example, we find five galaxies (VCC 0049, VCC 0220, VCC 222, VCC 0341, and VCC 0345) located 10–15 Mpc behind the main body of the Virgo cluster; these are all likely members of either the M cloud at $d \approx 31$ Mpc or the W cloud at ≈28.7 Mpc. The recession velocities of these

galaxies are also typically ≈1000 km s^{-1} larger than the mean recession velocity of Virgo.

The galaxies VCC 0648 and VCC 0657 are likely members of the Virgo W′ group, based on having measured distances similar to the value of ≈22.5 Mpc found for VCC 0731 (NGC 4365, the brightest and most massive W′ galaxy) and small angular separations from this galaxy. VCC 0199 may also be a member of the W′ group, based on its position and measured distance. However, its mean velocity is much closer to that of the W cloud galaxies; we therefore consider its membership uncertain. With the present data set, we do not find any significant difference in the mean distances to A, B, and C subclusters, and obtain a cluster depth of 2.4 ± 0.4 Mpc (omitting the W′ group and more distant structures).

Comparisons of our color and SBF measurements with predictions from SSP models are encouraging, both in supporting the adopted distance zero point and suggesting interesting possibilities for future stellar population studies using the full set of NGVS-SBF data. Future papers in this series will extend the catalog of SBF distances to fainter B_T magnitudes and bluer galaxies, where the single-color linear calibration is expected to be a poorer representation of the $\overline{M}_i$ versus color relation, and nonlinear calibrations, possibly involving multiple colors, will likely be required. The extended catalog will enable characterization of the 3D structure of the Virgo cluster and its various subcomponents to an unprecedented level of detail. Preliminary SBF distance moduli for three NGVS galaxies several magnitudes fainter than the current sample limit have already been presented by Paudel et al. (2017). These efforts are ongoing, and we expect to produce an eventual catalog of ≈250 SBF-based distances for galaxies observed in the NGVS.

This research has made use of the NASA/IPAC Extragalactic Database (NED) which is operated by the Jet Propulsion Laboratory, California Institute of Technology, under contract with the National Aeronautics and Space Administration. M.C., G.R., and J.P.B. acknowledge support from the PRIN INAF-2014 "EXCALIBURS: EXtragalactic distance scale CALIBration Using first-Rank Standard candles" project (PI: G. Clementini). J.P.B. gratefully acknowledges the hospitality of the Teramo Observatory. We thank John Tonry for the use of some software and helpful consultations.

Facility: CFHT (MegaPrime/MegaCam).

ORCID iDs

Michele Cantiello https://orcid.org/0000-0003-2072-384X
John P. Blakeslee https://orcid.org/0000-0002-5213-3548
Laura Ferrarese https://orcid.org/0000-0002-8224-1128
Joel C. Roediger https://orcid.org/0000-0002-0363-4266
Eric W. Peng https://orcid.org/0000-0002-2073-2781
Patrick R. Durrell https://orcid.org/0000-0001-9427-3373

References

Bertin, E., & Arnouts, S. 1996, A&AS, 117, 393
Binggeli, B., Popescu, C. C., & Tammann, G. A. 1993, A&AS, 98, 275
Binggeli, B., Sandage, A., & Tammann, G. A. 1985, AJ, 90, 1681
Binggeli, B., Tammann, G. A., & Sandage, A. 1987, AJ, 94, 251
Bird, S., Harris, W. E., Blakeslee, J. P., & Flynn, C. 2010, A&A, 524, A71
Blakeslee, J. P. 2012, Ap&SS, 341, 179
Blakeslee, J. P., Cantiello, M., Mei, S., et al. 2010, ApJ, 724, 657
Blakeslee, J. P., Jordán, A., Mei, S., et al. 2009, ApJ, 694, 556
Blakeslee, J. P., Lucey, J. R., Tonry, J. L., et al. 2002, MNRAS, 330, 443
Blakeslee, J. P., Vazdekis, A., & Ajhar, E. A. 2001, MNRAS, 320, 193
Boselli, A., Voyer, E., Boissier, S., et al. 2014, A&A, 570, A69
Cantiello, M., Biscardi, I., Brocato, E., & Raimondo, G. 2011a, A&A, 532, A154
Cantiello, M., Blakeslee, J., Raimondo, G., Brocato, E., & Capaccioli, M. 2007a, ApJ, 668, 130
Cantiello, M., Blakeslee, J. P., Raimondo, G., et al. 2005, ApJ, 634, 239
Cantiello, M., Brocato, E., & Blakeslee, J. P. 2009, A&A, 503, 87
Cantiello, M., Brocato, E., & Capaccioli, M. 2011b, A&A, 534, A35
Cantiello, M., Grado, A., Blakeslee, J. P., et al. 2013, A&A, 552, A106
Cantiello, M., Raimondo, G., Blakeslee, J. P., Brocato, E., & Capaccioli, M. 2007b, ApJ, 662, 940
Cantiello, M., Raimondo, G., Brocato, E., & Capaccioli, M. 2003, AJ, 125, 2783
Chen, C.-W., Côté, P., West, A. A., Peng, E. W., & Ferrarese, L. 2010, ApJS, 191, 1
Côté, P., Blakeslee, J. P., Ferrarese, L., et al. 2004, ApJS, 153, 223
Durrell, P. R., Côté, P., Peng, E. W., et al. 2014, ApJ, 794, 103
Durrell, P. R., Williams, B. F., Ciardullo, R., et al. 2007, ApJ, 656, 746
Feast, M., & Whitelock, P. A. 2014, in IAU Symp. 298, Setting the scene for Gaia and LAMOST, ed. S. Feltzing et al. (Cambridge: Cambridge Univ. Press), 40
Ferrarese, L., Côté, P., Cuillandre, J.-C., et al. 2012, ApJS, 200, 4
Freedman, W. L., & Madore, B. F. 2010, ARA&A, 48, 673
Freedman, W. L., Madore, B. F., Gibson, B. K., et al. 2001, ApJ, 553, 47
Ftaclas, C., Struble, M. F., & Fanelli, M. N. 1984, ApJ, 282, 19
Gavazzi, G., Boselli, A., Scodeggio, M., Pierini, D., & Belsole, E. 1999, MNRAS, 304, 595
Gwyn, S. D. J. 2008, PASP, 120, 212
Harris, W. E. 1991, ARA&A, 29, 543
Jordán, A., Blakeslee, J. P., Peng, E. W., et al. 2004, ApJS, 154, 509
Jordán, A., McLaughlin, D. E., Côté, P., et al. 2006, ApJL, 651, L25
Kelson, D. D., Illingworth, G. D., Tonry, J. L., et al. 2000, ApJ, 529, 768
Kim, S., Rey, S.-C., Jerjen, H., et al. 2014, ApJS, 215, 22
Lee, M. G., & Jang, I. S. 2017, ApJ, 841, 23
Magnier, E. A., & Cuillandre, J.-C. 2004, PASP, 116, 449
Makarov, D., Prugniel, P., Terekhova, N., Courtois, H., & Vauglin, I. 2014, A&A, 570, A13
Mei, S., Blakeslee, J. P., Côté, P., et al. 2007, ApJ, 655, 144
Mei, S., Blakeslee, J. P., Tonry, J. L., et al. 2005a, ApJS, 156, 113
Mei, S., Blakeslee, J. P., Tonry, J. L., et al. 2005b, ApJ, 625, 121
Paudel, S., Smith, R., Duc, P.-A., et al. 2017, ApJ, 834, 66
Press, W. H., Teukolsky, S. A., Vetterling, W. T., & Flannery, B. P. 1992, Numerical Recipes in FORTRAN The art of Scientific Computing (2nd ed.; Cambridge: Cambridge Univ. Press)
Raimondo, G. 2009, ApJ, 700, 1247
Raimondo, G., Brocato, E., Cantiello, M., & Capaccioli, M. 2005, AJ, 130, 2625
Reindl, B., Tammann, G. A., Sandage, A., & Saha, A. 2005, ApJ, 624, 532
Rejkuba, M. 2004, A&A, 413, 903
Rejkuba, M. 2012, Ap&SS, 341, 195
Robin, A. C., Luri, X., Reylé, C., et al. 2012, A&A, 543, A100
Roediger, J. C., Ferrarese, L., Côté, P., et al. 2017, ApJ, 836, 120
Sandage, A., Binggeli, B., & Tammann, G. A. 1985, AJ, 90, 395
Schlegel, D. J., Finkbeiner, D. P., & Davis, M. 1998, ApJ, 500, 525
Stetson, P. B. 1987, PASP, 99, 191
Stetson, P. B. 1990, PASP, 102, 932
Terlevich, A. I., & Forbes, D. A. 2002, MNRAS, 330, 547
Tonry, J., & Schneider, D. P. 1988, AJ, 96, 807
Tonry, J. L., Ajhar, E. A., & Luppino, G. A. 1990, AJ, 100, 1416
Tonry, J. L., Blakeslee, J. P., Ajhar, E. A., & Dressler, A. 1997, ApJ, 475, 399
Tonry, J. L., Dressler, A., Blakeslee, J. P., et al. 2001, ApJ, 546, 681
Trager, S. C., Faber, S. M., Worthey, G., & González, J. J. 2000, AJ, 120, 165
Villegas, D., Jordán, A., Peng, E. W., et al. 2010, ApJ, 717, 603
West, M. J., & Blakeslee, J. P. 2000, ApJL, 543, L27
Whitelock, P. A., Feast, M. W., & Van Leeuwen, F. 2008, MNRAS, 386, 313